

Molecular sized Eu-oxide clusters in defining optical properties in crystalline ZnO nanosponges

Soham Mukherjee,^{1,*} Sarmad Naim Katea,² Emille M. Rodrigues,³ Carlo. U. Segre,⁴ Eva Hemmer,³ Peter Broqvist,² Håkan Rensmo,^{1,*} Gunnar Westin^{2,*}

¹*Department of Physics and Astronomy, Ångström laboratory, Uppsala University, 75236 Uppsala, Sweden*

²*Department of Chemistry-Ångström, Ångström Laboratory, Uppsala University, 75121 Uppsala, Sweden*

³*Department of Chemistry and Biomolecular Sciences, University of Ottawa, 10 Marie Curie, Ottawa, Ontario, K1N 6N5, Canada*

⁴*Center for Synchrotron Radiation Research and Instrumentation and Department of Physics, Illinois Institute of Technology, Chicago, Illinois 60616, USA*

ABSTRACT: The detailed structure of ZnO doped with 5 at.% (metal) of the large aliovalent Eu^{3+} -ions was investigated using EXAFS to describe the local Eu and Zn coordination. The microstructure, crystalline phases, contents and ZnO unit-cell parameters for the ZnO:5%Eu sponges synthesised at 200 to 900 °C were obtained by XRD, SEM, and TEM analysis. XRD showed peaks solely of h-ZnO for the 600 °C sample, while heating at 700 °C and higher caused phase separation into h-ZnO:Eu and c- Eu_2O_3 . XRD showed a close to zero increase in ZnO unit cell-volume of ca. 0.4 vol%, compared to un-doped ZnO for the non-phase separated, clean oxide made at 600 °C. The Zn EXAFS data showed an almost intact local ZnO structure. The Eu EXAFS showed an unusually low coordination number (CN) of ca. 5 for the 200-600 °C samples, while the CN increased for higher temperatures, in concert with the formation of c- Eu_2O_3 . 23 DFT-generated theoretical ZnO structures containing Eu-clusters built from 1 to 4 Eu^{3+} - Zn^{2+} -vacancy- Eu^{3+} pairs were compared with the experimental data. The lowest formation energies and ZnO unit-cell volume increase versus un-doped ZnO (0.6-0.7 vol%), were obtained when combining two or four Eu^{3+} - Zn^{2+} -vacancy- Eu^{3+} pairs into Eu4 and Eu8 clusters showing an average Eu CN of ca. 5. These theoretically determined lowest energy structures were all in good agreement with the experimental results obtained by EXAFS and XRD. Photoluminescence excitation and emission spectra performed on the ZnO:5at%Eu sponges obtained at various temperatures, showed strong quenching of the characteristic Eu^{3+} transitions for samples obtained at 600 and 800 °C, most likely due to changes in the ZnO defect states, which are crucial for Eu^{3+} excitation, and due to self-quenching upon Eu clustering and c- Eu_2O_3 phase separation. Thus, the optical data further supported Eu clustering found by EXAFS, DFT and XRD techniques, corroborating structure-property relationships in these materials. Overall, as far as we can find, the findings reported herein point to a doping structure very different from those previously proposed in the literature. It demonstrates that the semiconductor ZnO can host molecular-sized clusters of metal-oxides, very dissimilar to ZnO.

1. Introduction

ZnO based semiconductors have gained enormous interest due to their potential as solar cells,(1-10) photo-catalysts,(11-14) diluted magnetic semiconductors,(15-17) piezoelectric nano-generators,(1,3) sensors,(1-3,18-22) opto-electronics,(1,2,18) green fuel catalysts,(23-27) and energy storage.(4,28-30) Doping with various metal ions has been extensively investigated to optimise the electronic structure or to endow ZnO with additional optical, magnetic or catalytic properties. However, in spite of an immense research effort over the last two decades there is a large variety of results reported on the properties of doped ZnO, some of them being even contradictory. This may to a great degree be related to the crystal quality, grain boundaries and perhaps most importantly, the doping structure (31-34), i.e. the spatial distribution and local coordination of the dopant-ions in the host lattice. In spite of this, there are few studies that describe the dopant structure in sufficient detail to connect properties with structure. To further complication, the structure and chemical contents vary with synthesis technique and heat-treatment, and have a profound effect on the optical and magnetic properties, as well as the electronic band-structure. A recent example is the study of ZnO:Co aiming for diluted magnetic semi-conductors (DMS), which showed promise for spin-polarised electron transport with potential to revolutionise the electronics industry.(15,16,35) In this area, the large number of reports give a scattered picture of the magnetic properties, and sometimes completely contradictory results. When investigating with atomistic probes, it was shown that the differences depended on the cobalt oxidation state, local formation of spinel $(\text{Zn,Co})_3\text{O}_4$ and clustering of Co^{2+} -ions residing at Zn^{2+} positions, yielding a paramagnetic

response from peripheral cobalt-ions.(36-43) This is a general finding applicable also to other oxide semiconductors, that strongly hampers the progress of e.g. solar hydrogen catalysts, as can be exemplified by the Ti-doped α -Fe₂O₃, showing very different properties depending on synthesis techniques; from improving the photo-catalytic activity to reducing it.(44)

Lanthanide (Ln)-doped semi-conductors, including ZnO have gained interest as potential photocatalysts or optoelectronic devices,(45-47) where the most studied system is Eu-doped ZnO. Some of the investigated materials contain unexpected high doping levels of up to 5% Eu and higher, when considering the much larger ionic radius and aliovalency of Eu³⁺ compared to the Zn²⁺-ions of the host lattice. Therefore, there has been an ongoing discussion on the reality and nature of such Eu-doped ZnO, not the least due the close to zero changes in XRD unit cell-dimensions observed with high levels of Eu³⁺ doping. A short review focused on the synthesis and connected properties is given in the in ref. (48) besides general reviews on Ln-doped ZnO and their properties and more comprehensive reviews are found in (45,47).

It has recently been proven beyond doubt, that the Eu³⁺ ions are situated within the ZnO nanocrystals when using synthesis temperatures from 200 to 700 °C.(48,49) In these studies, TG analysis, XRD, XPS, IR spectroscopy, SEM, TEM-ED/EDS, STEM-EELS mapping, and optical measurements were used to describe the chemistry and structure of Eu doped ZnO. It was found that at 200 to 500 °C, there were also minor amounts of organic residues or carbonate present, besides the Eu³⁺ ions. This is expected to be a general feature for chemically synthesised Ln doped ZnO samples, although, it is typically not investigated. For the 5%Eu samples, phase separation took place yielding nano *c*-Eu₂O₃ crystals at the surface of lesser Eu-doped ZnO. Hence, there exists a temperature window of clean, Eu-doped ZnO between 500 and 700 °C without any discernible phase separation or impurities. At lower Eu-doping levels of 0.5-1%, this window widened to reach up to 900 °C. It was also found, that in line with the literature, there were very small changes in XRD unit cell-parameters upon doping with the large Eu³⁺ ions. DFT modelling, using dimeric Eu³⁺ ion pairs flanking a metal vacancy for charge neutrality placed in the ZnO structure, did not result in any significant reduction of the unit cell-volume, compared to a linear Vegard type model using the calculated ionic radius of 83.5 pm for four coordinated Eu³⁺ ions.(48) This indicates that while it might seem possible for the flanking Eu³⁺ ions to make use of the Zn²⁺-ion vacancy void between two Eu³⁺ ions, the surrounding ZnO lattice would be compressed around the site, resulting in increased ZnO cell-parameters resulting in a small energy gain compared to larger clusters.

Thus, while it was shown that the Eu³⁺ ions resided within the ZnO crystals, without a clearly visible phase separation in TEM imaging or XRD analysis, their local dopant structure remained unknown. Therefore, to be able to understand how the large amounts of the big Eu³⁺ ions can be introduced into the ZnO phase, without changing the ZnO unit cell-volume, a more detailed study on the 5%Eu-doped ZnO was conducted using EXAFS. This technique allows to describe the local Eu³⁺-

and Zn^{2+} -ion coordination numbers, bond-lengths, and neighbouring conditions. These data were compared with DFT modelling, using 23 Eu^{3+} - Zn^{2+} vacancy - Eu^{3+} (abbreviated as Eu^{3+} - $\text{Zn-vac.}-\text{Eu}^{3+}$ hereafter) pair-based clusters of sizes up to 8 Eu^{3+} ions. Their calculated Eu coordination number, Eu-Eu distances, ZnO unit cell-volume and total energy were compared with the experimentally obtained local structures obtained from EXAFS data and the close-to-zero volume expansion in ZnO unit cell-parameters found by XRD analysis. A very good agreement between the theoretical and experimental data was found for three clusters containing four or eight Eu-ion membered clusters. This allows to understand the unexpected doping structure and how the ZnO unit cell-dimensions can be retained on doping with high levels of large, alio-valent ions such as Eu^{3+} .

Furthermore, the changes in coordination over the temperature range, 200 to 900 °C, were examined to follow the Eu-dopant coordination; from the lowest synthesis temperature of 200 °C, to the clean, Eu-doped oxide obtained at 600 °C, and further into the temperature range, 700-900 °C, where the Eu is expelled from the ZnO to yield 5-10 nm sized *c*- Eu_2O_3 particles on the ZnO sponge surface. The Eu-doped ZnO microstructures were also further described with SEM and TEM imaging, although more thorough microscopy studies, including TEM-EELS mapping has been provided elsewhere.^(48,49) The optical studies provided insight into the energy levels and properties of the minor defects in these materials, not accessible by the TEM and EXAFS probes.

Based on the results obtained in this study, highly complex and to-date unforeseen molecular-like dopant structures are proposed that may shed light on various hard to explain magnetic and optical data for this kind of semi-conductor materials. The findings reported herein also point to a general possibility to form clusters of “misfit”-ions within rigid semi-conductor structures for the design of optical, magnetic, catalytic and transport properties, where typically a high dopant level is desired, while the semi-conductor properties are sensitive to disturbances in the semi-conductor lattice.

2. Experimental section

2.1. Chemicals and synthesis. All chemicals were used as received. The actual molecular weights of the hydrated salts were determined gravimetrically as Eu_2O_3 , after heating at 1000 °C for at least 3 h. Nanosponges of undoped ZnO and doping with 5 mol% Eu in ZnO, were synthesised as given in detail in reference.^[46] Briefly, zinc-dinitrate-hexahydrate ($\text{Zn}(\text{NO}_3)_2 \cdot 6\text{H}_2\text{O}$, Sigma-Aldrich >99%), zinc-diacetate-dihydrate ($\text{Zn}(\text{OAc})_2 \cdot 2\text{H}_2\text{O}$, Sigma-Aldrich >99%) and triethanolamine (TEA, Sigma-Aldrich p.a) in methanol (Scharlau, 99.5%) was mixed with an appropriate amount of europium-trinitrate-pentahydrate (Aldrich 99.9%, $\text{Eu}(\text{NO}_3)_3 \cdot 5\text{H}_2\text{O}$ and triethanolamine (TEA), in methanol (Scharlau, analytical grade 99.9%). Subsequently, the solution was evaporated to a transparent or whitish paste on a Petri-dish and heated for 3 min in a muffle furnace set to 200, 400, 600, 700, 800, or 900 °C. Upon heating to 200 °C or higher temperatures, very light voluminous ZnO or ZnO:Eu sponge powders were formed.

2.2. Sponge microstructure by XRD, SEM, and TEM. The crystallinity of pure and Eu-doped ZnO, obtained by heating the precursor paste for 3 min at temperatures between 200 and 900°C, was studied with powder X-ray diffraction (XRD) analysis using Cu K_α radiation. The phase contents, unit cell-parameters, and crystal sizes were determined with the Topas software. The following cif-files were employed: ZnO (PDF Card 00-036-1451, hexagonal ZnO, space group $P6_3mc$) and Eu₂O₃ (PDF Card 00-034-0392, cubic Eu₂O₃, space group $I-a3$). The overall microstructure of the nanosponges was studied with a Zeiss Merlin field emission gun scanning electron microscope (SEM), while the detailed microstructure was studied with a JEOL 2100F transmission electron microscope operated at 200 kV (TEM).

2.3. Local structure by EXAFS. Room temperature Extended X-ray Absorption Fine Structure (EXAFS) measurements were performed at the Materials Research Collaborative Access Team (MRCAT) bending magnet beamline (Sector 10) at Argonne National Laboratory's Advanced Photon Source. The MRCAT bending magnet beamline uses a water-cooled Si (111) double crystal monochromator and collimating slits for energy selection and optimal energy resolution. EXAFS measurements were performed in transmission mode at the Zn K and Eu L₃ edges for the ZnO:5%Eu nanosponges prepared at 200, 600, 700, 800, and 900°C. The amount of sample was adjusted to yield a total absorption coefficient (μx) of around 2.5 after the edge in order to ensure a linear response. Measured quantities of powdered sample, amounting to ca. 40 mg, were thoroughly mixed with boron nitride and pressed into 10 mm diameter pellets which were and mounted in Kapton tape for EXAFS measurements. A Zn foil was measured with each scan as reference to track any energy shift between the scans. The reference energies obtained were used for edge alignment during the data processing. Commercial Eu₂O₃ was used as Eu reference material, while the elemental reference was calibrated using an Fe foil. Each scan was taken with a step of 5 eV in the pre-edge region, 0.2 eV in the XANES (-50 eV to +50 eV) region and 2 eV for the rest of the scan. The number of scans was decided based on the statistics. Typically, for a given sample. EXAFS data were analysed by the IFEFFIT interactive XAFS data analysis package, using AUTOBK for background subtraction and the FEFF6 program for calculating theoretical scattering amplitudes and phases for a pair of atoms, using the input file prepared by ATOMS program that uses the standard crystallographic data. For each measured X-ray absorption spectrum, the EXAFS signal $\chi(k)$ was extracted using AUTOBK. $\chi(k)$ is generally defined as:

$$\chi(k) = \sum_j \frac{N_j S_0^2 f_j(k) e^{2R_j/\lambda_j(k)} e^{-2k^2 \sigma_j^2}}{k R_j^2} [\sin 2k R_j + \delta_j(k)]$$

where k is the photoelectron wavenumber, $f_j(k)$ and $\phi_j(k)$ represent the photoelectron back-scattering amplitude and phase for the j^{th} shell, $\lambda_j(k)$ is the photoelectron inelastic mean free path, N_j , R_j , and σ_j^2 represent the coordination number, interatomic distance and mean-square disorder in R_j (j^{th} coordination shell), and S_0^2 the amplitude reduction factor. Multiple scans for each edge were properly aligned, merged and normalised, using Athena software. The background below $R_{bkg} = 1.0 \text{ \AA}$ was

minimised by using the built-in AUTOBK algorithm. The final merged scans for each metal edge were simultaneously analysed, using the theoretical fitting standards computed with FEFF6 software. Input for FEFF was prepared using the ATOMS program and the crystallographic data. The data were analysed using FEFFIT software. The errors were estimated by a standard Levenberg-Marquardt, non-linear minimization of the statistical χ^2 parameter, built within the FEFF6 program. Fits to all data in k and R (real part and magnitude) space, extracted EXAFS parameters and their associated error limits are detailed in the Supporting Information.

2.4. Cluster modelling by DFT. The electronic structure calculations performed in this work are based on density functional theory (DFT) in the implementation with plane waves and pseudopotentials. The exchange-correlation energy contribution to the total energy was modelled using the density functional proposed by Perdew-Burke-Ernzerhof (PBE)^(50,51) Projector Augmented Wave (PAW) pseudo-potentials^[52,53] describing explicitly 4, 12 and 9 electrons were used for O($2s^2p^4$), Zn($3d^{10}4s^2$) and Eu($4f^65d^15p^66s^2$), respectively. For Eu, the chosen pseudo-potential has earlier been used to accurately describe the Eu^{3+} oxidation state. In the current investigation of Eu-dopants in ZnO, explicit effects of spin-polarisation in the Eu^{3+} ions were not accounted for. All calculations were performed using the Vienna Ab Initio Simulation Package (VASP).^[54-57]

The bulk hexagonal ZnO (*h*-ZnO) host was modelled using an orthorhombic representation of the hexagonal ZnO as basis, with a unit cell size of $9.86 \times 10.60 \times 11.38 \text{ \AA}^3$, containing in total 48 ZnO units, as obtained from the cell optimisation at the current level of theory. Upon Eu-doping, the same unit cell was used to construct supercell structures, always ensuring that the doping concentration was kept constant at 4.17 at% Eu with respect to the total number of metal ions in the stoichiometric ZnO. The cut-off energy, truncating the plane-wave basis set, was set to 600 eV, and the k -point sampling of the Brillouin zone was kept at correspondingly a $3 \times 3 \times 3$ k -point sampling, using the Monkhorst-Pack scheme, for the smallest unit cell. Optimisation of position of the ions and cell volumes were performed for all presented structures until the largest force on each atom was smaller than 0.001 eV/atom. Along with total energy evaluations, radial distribution functions (partial and full) were computed to allow for comparison to the results concerning distances and coordination numbers obtained from the experimental EXAFS data.

2.5. Optical properties. Excitation and emission photoluminescence spectra were obtained using a Horiba QuantaMasterTM 8075-21 spectrofluorometer, equipped with a double additive excitation monochromator with triple gratings, a single emission monochromator with triple gratings, and a UV-VIS PMT detector (Hamamatsu PMT R928). The excitation source used for the recording of steady-state excitation and emission spectra was a 75 W continuous Xenon lamp, while a 450 W pulsed Xenon lamp was used for the time-resolved emission spectra. All samples were analysed at room temperature,

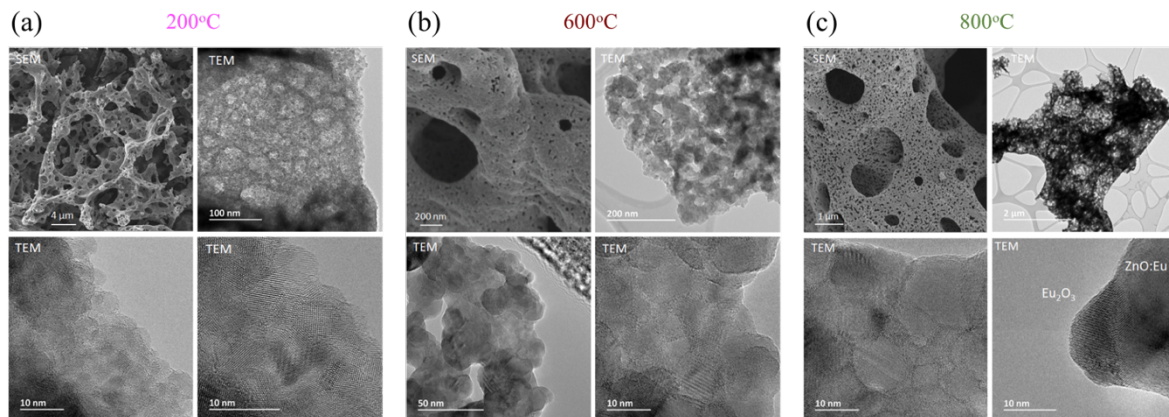


Figure 1. SEM and TEM images of ZnO:5%Eu sponges heated for 3 min at (upper figure) 200 °C, (mid figure) 600 °C, and (lower figure) 800 °C.

in solid-state as pressed pellets between 1 mm thick quartz windows using a 90 ° configuration between the excitation beam and emission collection.

3. Results and Discussions

3.1. Sponge microstructure by XRD, SEM and TEM

The synthesis of sponge structures, built of nano-crystallites, was previously reported in detail.(48,49,58) In the present study, ZnO and ZnO:5%Eu nanosponges were prepared by heating a precursor paste for 3 min at 200, 400, 600, 700, 800, and 900 °C, in air. SEM and TEM images showing the microstructures of the ZnO:5%Eu sponges, obtained after heating at 200, 600, and 800 °C, respectively, are shown in Figure 1.

The ZnO:5%Eu nanosponge obtained at 200 °C contained minor amounts of organic residues, including carboxyl groups, while heating at 400 °C left only minor amounts of carbonate.(48) Heating at 600 °C, removed all residues to yield a pure, Eu-doped zinc-oxide sponge without detectable phase segregation.(48,49) On heating at 700 °C, the first very minor phase segregation was observed by TEM (Figure 1), while it was hard to detect in the XRD (Figure 2). After heating at 800 °C, the cubic-Eu₂O₃ phase was clearly segregated at the ZnO sponge surface as ca. 5-10 nm sized particles, as shown by TEM and XRD (Figure 1 and 2). The XRD phase analysis indicated that ca. 50 and 30 wt% of the Eu remained in the ZnO at 800 and 900 °C, respectively. The Bragg reflections corresponding to ZnO and Eu₂O₃ are indexed in Figure 2(a), corresponding to reference ZnO (PDF Card – 00-036-1451) and Eu₂O₃ (PDF Card – 00-034-0392) data. From the TEM images, it can be observed that the ZnO grain connectivity was more intimate for the 600 and 800 °C sponges showing a complete interface between the ZnO:Eu grains, compared with that of the 200 °C sponge, which showed more rounded, less tightly connected grains.

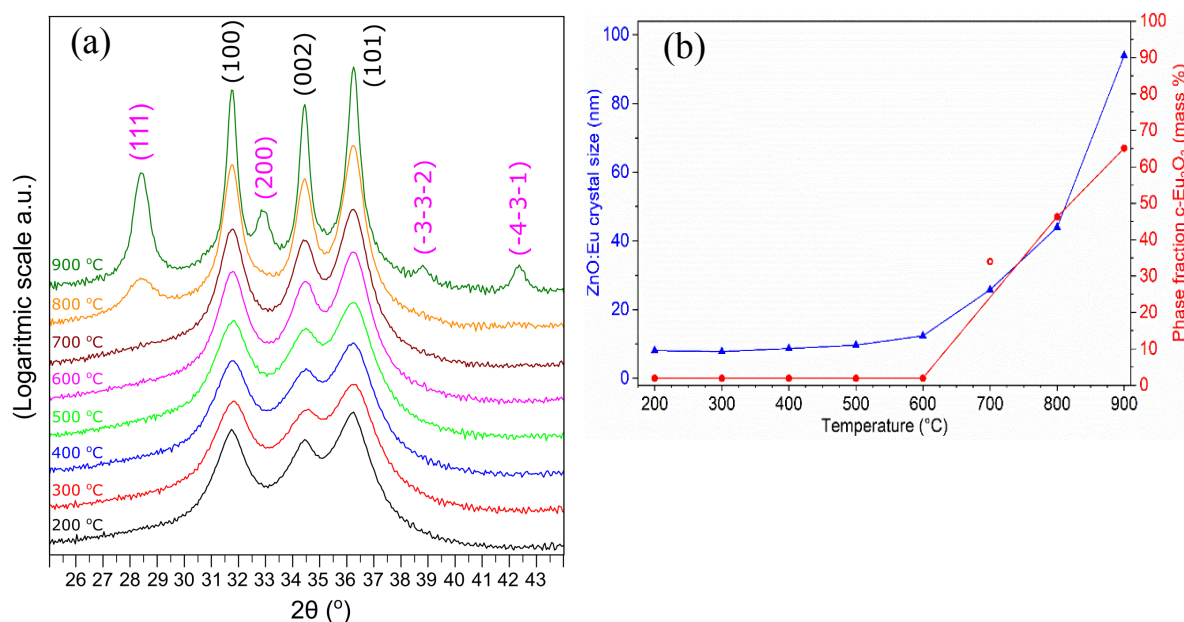


Figure 2. (a) XRD patterns *versus* temperature graph of ZnO:5%Eu sponges heated for 3 min at 200, 300, 600, 700, 800, and 900 °C, showing the emergence of the *c*-Eu₂O₃ phase. (b) A graph of the XRD derived approximate mass fraction of Eu₂O₃ in the ZnO:Eu sponge and XRD derived ZnO:Eu crystal size *versus* temperature.

3.2. Local structure of the ZnO:5%Eu sponges by EXAFS

EXAFS. The element selectivity of the EXAFS technique allows to probe to the local environment of the host and dopant ions separately, which is essential for the understanding of especially the Eu-dopant structure. ZnO and ZnO:5%Eu nanosponges prepared by heating for 3 min at 200, 400, 600, 700, 800, and 900 °C, respectively, were studied with EXAFS, along with *c*-Eu₂O₃ for comparison.

Zn environment. Figure 3a shows $\chi(k)$ functions for the Zn K edge in the ZnO:5%Eu ZnO nanosponges. The $\chi(k)$ oscillations remained well-defined up to high photoelectron wavenumbers of $k \sim 14 \text{ \AA}^{-1}$, which indicates a high degree of short-range order in the Zn environment. The major frequency components of the $\chi(k)$ functions appeared quite similar to that of pure ZnO, indicating that the presence of Eu did not modify the local environment around Zn to any appreciable degree. The $\chi(k)$ amplitudes increased with synthesis temperatures from 200 to 900 °C, which may to some extent be related to the increasing crystallite sizes with increased synthesis temperatures in the range 700 to 900 °C. The main dampening however, was found for the 200 and 600 °C samples, for which the crystal sizes were fairly small ($\sim 10 \text{ nm}$), as given by Figure 1. In addition, formation of cavities hosting Eu-oxide clusters within the ZnO crystals can effectively act as grain boundaries, and thereby reduce the long-range ordering (*vide infra*). Synthesis temperatures above 600 °C would reduce the amount of such cavities when *c*-Eu₂O₃ is expelled from the ZnO grains. Thus, the dampening of the $\chi(k)$ amplitudes likely has different origins in the low ($< 600 \text{ °C}$) and at high ($> 600 \text{ °C}$) temperature regimes.

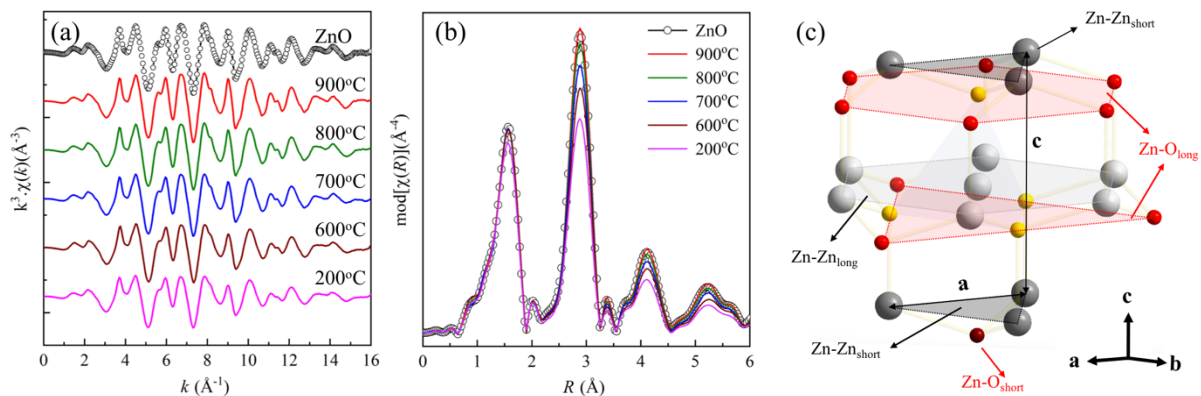


Figure 3. (a) Zn-K $\chi(k)$ functions and (b) corresponding Modulus of $\chi(R)$ functions for ZnO:5%Eu nanospices synthesised at 200, 600, 700, 800 and 900 °C, and undoped *h*-ZnO for comparison, (c) Spatial distribution of 1NN (4O: yellow), 2NN (6Zn-Zn_{short}: dark grey, 6Zn-Zn_{long}: light grey) and 3NN (1Zn-O_{short}: dark red, 9Zn-O_{long}: red) atoms (NN: near neighbouring).

The dampening effects were more evident in Figure 3b, where the individual frequency components of $\chi(k)$ functions were isolated by Fourier transforming (FT) the data to corresponding $\chi(R)$ functions. The peaks observed in the $\text{mod}[\chi(R)]$ functions correspond to scattering from near neighbouring (NN) atoms occurring at different distances from a central Zn atom ($R = 0$ Å). Zn EXAFS parameters were extracted by fitting the $\chi(R)$ data over the range 1.1 - 3.5 Å using a Hanning window. Details of the fitting procedures applied and local parameters extracted are provided in the Supporting Information Table S1. An overlay plot of the real part of the $\chi(R)$ functions and their corresponding fits are shown in Figure S1. The 1NN environment revealed three short and one slightly longer Zn-O bonds (Table S1), typical of an asymmetric Zn-O₄ tetrahedral unit in hexagonal ZnO. The CN slightly below four for the 1NN for the 200 °C sample is likely due to surface effects, due to the smaller particle sizes and rounder shape providing less inter-ZnO grain contacts, exhibiting oxygen-poor faces, and cavities containing Eu-O clusters interrupting the ZnO crystal, as well as the presence of organic residues.

The second EXAFS peak observed in Figure 3b includes contributions from 2NN (the Zn, Eu coordination shell) and 3NN (the next O coordination shell). Spatial distributions of 2NN (6 short Zn-Zn and 6 long Zn-Zn) and 3NN (1 short, 6 medium and 3 long Zn-O) interatomic distances are shown in Figure 3c. The coordination numbers of Zn ($n_{\text{Zn-Zn}}$), Eu ($n_{\text{Zn-Eu}}$) and O atoms ($n_{\text{Zn-O}}$) surrounding a Zn atom extracted from EXAFS analysis are shown Figure 4a. The sum of $n_{\text{Zn-Zn}}$ and $n_{\text{Zn-Eu}}$ gives the total 2NN coordination number ($n_{2\text{NN}}$) around Zn. Figure 4a reveals that starting from a lower CN ($n_{2\text{NN}}$ of ca. 10), the $n_{2\text{NN}}$ increased with increasing annealing temperature approaching the ideal bulk limit value of 12 (pure ZnO). Lower $n_{2\text{NN}}$ values cannot be explained by competing Zn-Zn and Zn-Eu interactions alone, but are most likely due to a size effect, and hence more prominently observed for higher NN than 1NN (O-shell). Since Zn EXAFS provides volume-averaged local information about all Zn atoms,

smaller average crystallite sizes occurring at lower temperatures would be reflected locally in the lowering of n_{2NN} and n_{3NN} values.

The n_{Zn-Eu} values are close to the low nominal value of 0.05, which prompted us to also model the Zn-K EXAFS data without any contribution from Eu. A comparative error analysis (Table S2) indeed revealed the models to be rather similar. This test confirmed that Eu-doping did not significantly alter the hexagonal ZnO lattice locally, but only reduced the short-range order at lower temperatures; an effect connected to cavities occupied by Eu-oxide clusters. This also explains why larger uncertainties were observed when estimating the coordination numbers and interatomic distances for the Zn-Eu pairs (Figure 4), where the largest uncertainties were observable for the 900 °C nanosponges in which the Zn-environment contains a smaller amount of Eu.

The Zn-Zn, Zn-Eu and Zn-O interatomic distances are plotted in Figure 4b. The average Zn-Eu interatomic distances were ca. 0.2 Å longer than the Zn-Zn distances, as expected considering that the Eu^{3+} ions have estimated ionic radii of 84, 89, and 95 pm for CN = 4, 5, and 6, respectively,(46) compared to 60 pm for tetrahedral Zn-ions.(59) Interestingly, while the synthesis temperature hardly affected the Zn-Zn and short Zn-O distances of the host ZnO, the Zn-Eu and long Zn-O (3NN) distances decreased with increasing temperature, more evidently over the 700°C to 900°C range. It is in this temperature range that the zinc coordination around the Zn atoms increased to resemble that of pure bulk ZnO, with almost constant Zn-Eu coordination numbers (Figure 4a). These observations are in concert with the XRD and TEM data, revealing expulsion of Eu from the ZnO:Eu grains forming *c*- Eu_2O_3 particles on the surface (Figure 1b,c). These changes were accompanied by a very small decrease in ZnO unit cell-volume, yielding a material with only 30-50 wt% of the Eu-oxide residing within the ZnO grains at 800 to 900 °C (Figure 1 and 2). The mobility of the metal-ions in this temperature range was also displayed by a fast ZnO grain-growth, from ca. 10 nm at 200-600 °C to 94 nm at 900 °C, as shown in Figure 2b.

These observations indicate that the Eu^{3+} ions cluster within the ZnO, while not affecting the general ZnO lattice to any large degree, and that ZnO:Eu suffers phase separation into lower Eu content ZnO:Eu and *c*- Eu_2O_3 at elevated temperatures.

Eu environment. The local environment around the Eu dopant ions provides experimental insight into the cluster-structure within the ZnO crystals, which cannot be obtained by the other techniques used. An overlay plot of the $\chi(k)$ functions for Eu-doped ZnO prepared at different synthesis temperatures as well as *c*- Eu_2O_3 , for comparison are presented in Figure 5a. The Eu-L₃ EXAFS for the nanosponges prepared at 900°C appears similar to that of *c*- Eu_2O_3 with well-defined $\chi(k)$ oscillations extending up to $k \sim 11.0 \text{ \AA}^{-1}$. The $\chi(k)$ function based on the experimental data becomes slightly less well-defined for the 800 °C sponge and even more so for lower temperatures resulting in a k_{max} of ca. 8.5 \AA^{-1} . This, thus suggests a higher disorder in the Eu local environment for these samples, compared to their Zn $\chi(k)$ counterpart.

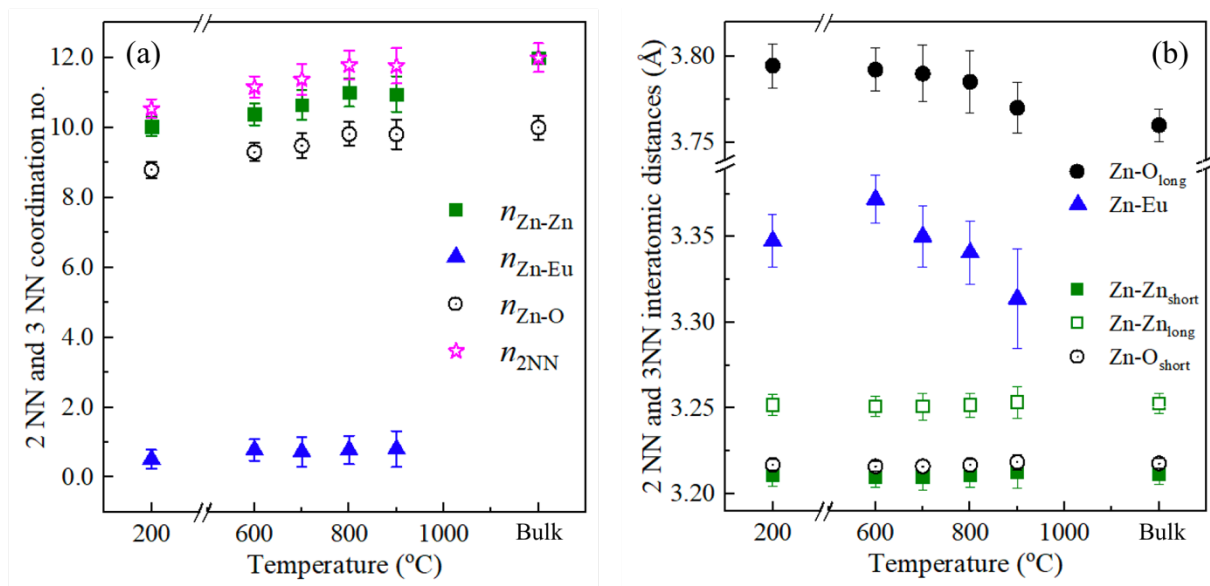


Figure 4. (a) Coordination number of Zn, Eu, 2NN (Zn+Eu) and 3NN (O) about a Zn atom; (b) Interatomic distances between Zn-Zn short (red open circles), Zn-Zn long (red closed circles), Zn-Eu (blue triangles), Zn-O short (black open squares), Zn-O long (black closed squares).

The differences in Eu- L_3 $\chi(k)$ functions were clearly manifested in the FT of these three compounds, as shown in Figure 5b. It is immediately noticeable that the 1NN peaks for Eu $\chi(R)$ appear at longer R -values compared to the 1NN peaks for Zn $\chi(R)$, as expected from the smaller ionic radius of the Zn^{2+} -ion compared to the Eu^{3+} ion. The 1NN peaks for Eu $\chi(R)$ appeared relatively broad and showed stronger intensity variations, suggesting that the Eu atoms assumed very varied Eu-O coordination environments. The higher NN features, contributed by Eu and Zn, were dampened when comparing the 900 °C sample with the 800 °C sample, and became rather diffuse in the temperature regime 200-700 °C. This is interpreted as due to surface effects, interference between Eu-Eu and Eu-Zn, and local inhomogeneities. Increased ordering of the Eu local structures with increased synthesis temperature from 700 °C to 900 °C is in consonance with the formation of all six coordinated Eu in the $c\text{-Eu}_2\text{O}_3$, concluded from XRD and TEM data.

Local structural information about Eu was obtained by fitting the EXAFS data over the range 1.1 - 4.2 Å. An overlay of the real part of the $\chi(R)$ functions and their corresponding fits are presented in Figure 5c. Several possibilities of ZnO-Eu host guest interactions were considered for comparison with doping models used in the literature; metal-site substitution, interstitial doping, local clustering, and phase segregation. The Supporting Information contains further details of the EXAFS analyses and local parameters extracted from these fits (Table S2). The description of 1NN required two different Eu-O bonds, as given in Table S2. Using a single Eu-O path increased the σ^2 values, indicating that these contributions needed to be accounted for separately. The peak broadening observed in Figure 5b is therefore due to an intrinsically larger spatial distribution of Eu-O distances in the 1NN environment.

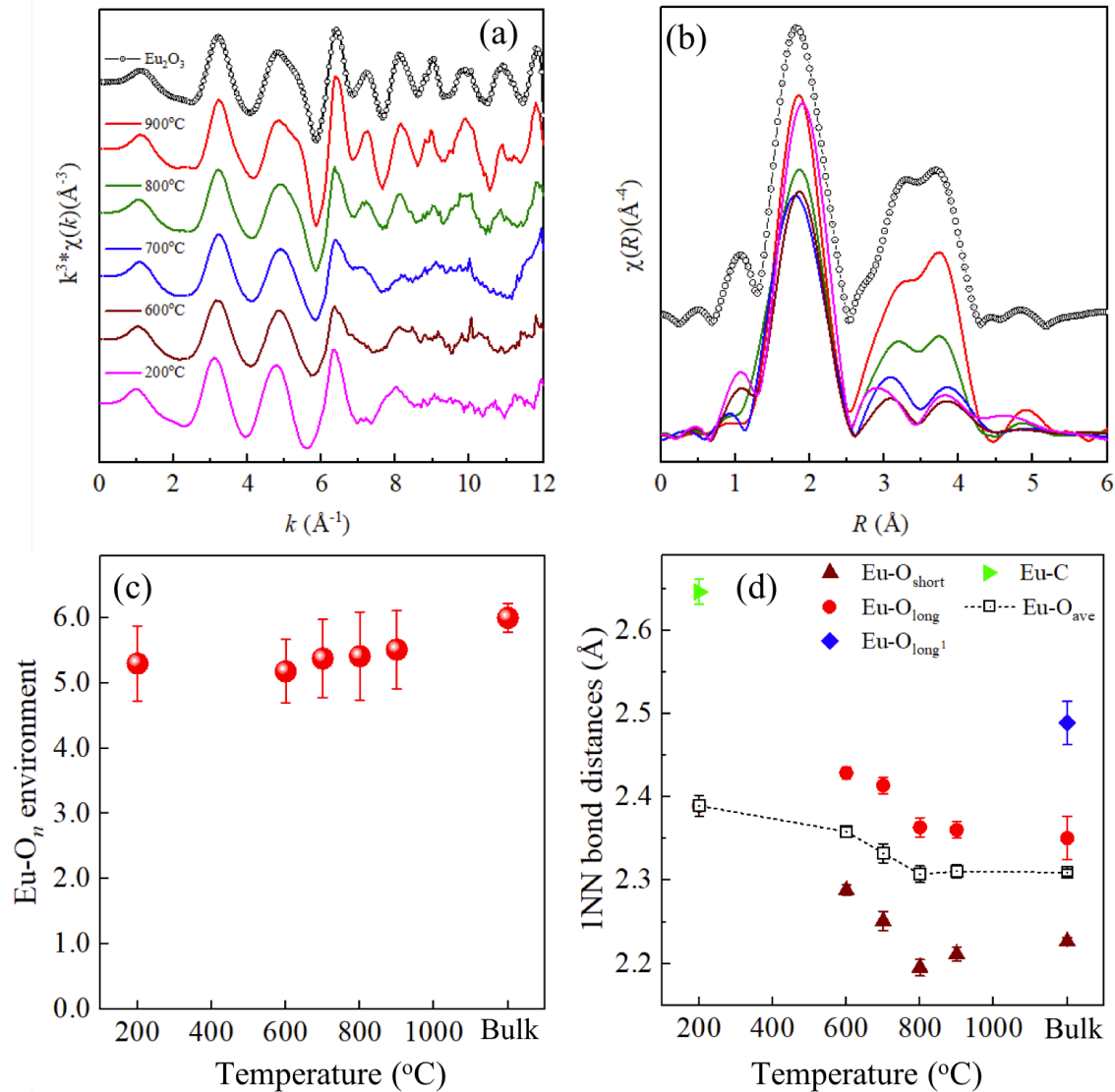


Figure 5. (a) Eu-L3 $\chi(k)$ functions and (b) corresponding modulus of $\chi(R)$ functions the for Eu-doped ZnO nanosponges synthesised at 900 °C (red), 800 °C (olive), 700 °C (blue), 600°C (wine) and 200 °C (magenta), respectively compared to bulk c - Eu_2O_3 (black circles). (c) Evolution of number of O atoms bonded to Eu in Eu-doped ZnO nanosponges synthesised at different annealing temperatures. (d) Eu-O bond distribution in Eu doped ZnO nanosponges synthesised at different temperatures. Corresponding average Eu-O bond distances for each annealing temperature are represented by the black open squares.

The extra intensity in the 1NN peak at ca. 2 Å for the 200 °C sample (Figure 5b), could not be accounted for by interstitial Zn or Eu doping. Instead, it could stem from organic residues, such as carboxylate groups, not fully removed at 200 °C, as described in earlier studies using TG, XPS and IR spectroscopy.⁽⁴⁶⁾

The description of the 1NN environment (Eu-O_n) around Eu are given in Figure 5c,d, in terms of average coordination number of O bonded to Eu and Eu-O bond distances. Eu^{3+} ions typically attain

coordination numbers of 6-8.⁽⁵⁹⁾ For pure Eu_2O_3 , CN 6 is expected for $c\text{-Eu}_2\text{O}_3$. Figure 6a shows that the 200 and 600 °C sponges assumed CN close to 5, which is very unusual for any Ln^{3+} -ion. Heating at temperatures of 700 °C and higher increased CN towards six for the 900 °C sample. This is in line with the formation of $c\text{-Eu}_2\text{O}_3$ having CN 6, as shown by XRD and TEM. The CN lower than six, found in the 900 °C sample, is reasonable knowing that ca. 30 % of the Eu was still present in the ZnO grains and that the $c\text{-Eu}_2\text{O}_3$ forms small nanoparticles with a large surface area, where the Eu at the surface may have a CN lower than six.

Figure 5d shows 1NN distances for all nanosponges. The 200 °C sample showed an average Eu-O bond length of 2.39 ± 0.01 Å, while the 600 °C sample showed a slightly shorter average bond length of $2.36 \text{ Å} \pm 0.01$, which could be due to some organic groups being coordinated to the Eu^{3+} ion in the former case. From 700 °C and up, a decrease in average Eu-O bond-length was observed, eventually attaining close to the ideal Eu-O distances for pure $c\text{-Eu}_2\text{O}_3$ for 800°C and 900°C. Average Eu-O distances, therefore are significantly longer (~ 0.4 Å) than Zn-O bond distances (~ 1.96 Å). This observation, along with a CN over 5 completely rule out the possibility of Eu acting as a pure substitutional (60-63) impurity (CN = 4) at Zn sites in the $h\text{-ZnO}$, regardless of synthesis temperature. The O-shell description from EXAFS neither fits the possible configurations of interstitial doping: tetrahedral voids occurring at (0,0,3/8), (0,0,5/8), (2/3,1/3,1/8) and (2/3,1/3,7/8), and (b) octahedral voids: (1/3,2/3,1/4) and (1/3,2/3,3/4) nor typically higher coordination numbers of Eu (59), as elaborated in the Supporting information. Thus, from Figures 5c and 5d, it is evident that Eu adopts a bigger, more disordered coordination environment and such mode of doping does not fit any of the generally proposed models for Ln doping in ZnO.

Estimation of absolute coordination numbers of Zn ($n_{\text{Eu-Zn}}$) and Eu ($n_{\text{Eu-Eu}}$) surrounding an Eu atom from higher NN peaks is non-trivial. This arises from the difficulty in decoupling the effects of surface and disorder from the strongly damped $\chi(R)$. Instead, an estimate of the relative fraction of Zn ($f_{\text{Eu-Zn}}$) and Eu atoms ($f_{\text{Eu-Eu}}$) surrounding an Eu atom is provided in Figure 6a. The reference for Eu considered here is $c\text{-Eu}_2\text{O}_3$, so the model of the Eu environment was achieved with a 1:1 distribution of short and long Eu-Eu correlations and one Eu-Zn correlation, as already obtained from fitting the Zn EXAFS data. If Eu^{3+} ions were doped homogeneously throughout the ZnO lattice, the ideal value for $f_{\text{Eu-Eu}}$ would be 0.05, considering the nominal doping percentage of 5 % Eu. Figure 6a clearly shows $f_{\text{Eu-Eu}}$ values to be significantly higher than 0.05, indicating clustering of Eu in the ZnO matrix. A closer inspection reveals that for the 200-700 °C samples the $f_{\text{Eu-Zn}} : f_{\text{Eu-Eu}}$ ratio stays close to 1:1, but for the 700-900 °C samples the $f_{\text{Eu-Zn}} : f_{\text{Eu-Eu}}$ ratio steeply increases to reach ca. 0.75 for the 900 °C sample. This is in concert with the ca. 70 wt% $c\text{-Eu}_2\text{O}_3$, obtained by XRD. The ca. 1:1 ratio of Eu-Eu and Eu-Zn pairs found for the 200-700 °C samples indicate that the clusters have to be small to minimise the number of Eu-O-Eu bonds. Since the amount of Eu in the sponges was constant over temperature, an increase in

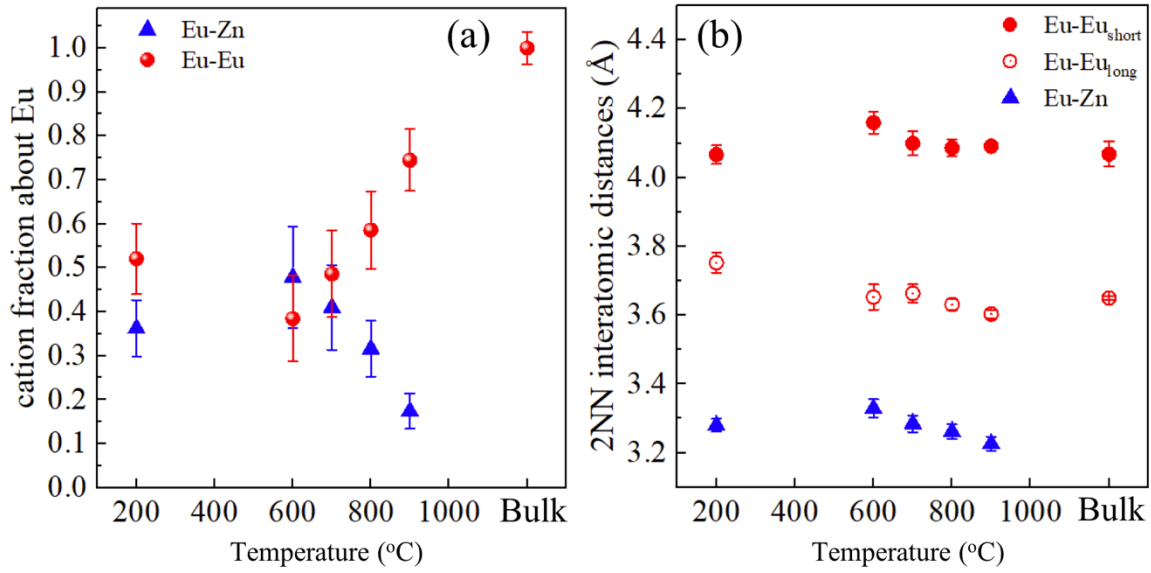


Figure 6. (a) Fraction of Zn and Eu bonded to Eu, showing the Eu clustering to increase with temperature. (c) Interatomic Eu-Eu_{short}, Eu-Eu_{long}, and Eu-Zn (same as Zn-Eu), showing a larger spatial distribution of the cationic sub-lattice compared to Zn.

$f_{\text{Eu-Eu}}$ at the expense of $f_{\text{Eu-Zn}}$ means that on average, the Eu atoms got more assembled, as expected from the formation of $c\text{-Eu}_2\text{O}_3$ particles, from 700 °C. This does not rule out that, at the same time, fewer, less assembled clusters may form, such as $\text{Eu-Zn}_{\text{vac.}}\text{-Eu}$ clusters within the ZnO grains.

Figure 6b shows the interatomic distances between Eu-Eu and Eu-Zn atom pairs, ranging from 3.3 Å to 4.2 Å. This distribution of metal-metal distances in Eu local environment is larger (ca. 0.9 Å) compared to the distribution of metal-metal distances in Zn local environment (ca. 0.2 Å, ranging from 3.2 Å – 3.4 Å). Such large disorder in the mixed cation sub-lattice around Eu^{3+} ions explains the more prominent dampening effects observed for Eu-L₃ $\chi(R)$ (figure 5b), compared to Zn-K $\chi(R)$ (Figure 3b). The Eu-Eu distances decreased gradually in the temperature regime 600 to 900 °C, approaching their ideal values in bulk $c\text{-Eu}_2\text{O}_3$. Similar trends were observed for Zn-Eu and longer Zn-O distances in Figure 4b.

General features of the overall structure. The large ionic radius difference between Zn^{2+} - and Eu^{3+} ions should render Eu incorporation at ideal Zn lattice sites or interstices in the $h\text{-ZnO}$ structure energetically unfavourable. The Zn-K EXAFS data showed a close to unchanged $h\text{-ZnO}$ (undoped) structure upon doping with as high amounts as 5% Eu. Thus, this is corroborated by the XRD data showing a very small increase of ca. 0.4% in ZnO unit cell volume. This conforms to a structure with small Eu-oxide clusters, not easily detected with XRD and TEM, residing in cavities within the ZnO crystals. The Eu EXAFS showed very unusual low Eu oxygen coordination numbers close to five for samples heated at 200-700 °C. At higher synthesis temperatures the Eu CN increased to approach six for the 900 °C sample, in line with a phase separation forming $c\text{-Eu}_2\text{O}_3$ observed experimentally. The

local Eu-O coordination environments indicated a wide distribution of bond-lengths in all cases. For the higher temperatures, this is likely due to the presence of two phases; ZnO:Eu and *c*-Eu₂O₃, while for the lower temperature samples, it points towards the presence of Eu-oxide clusters, highly disordered in bond lengths and angles, as well as very low Eu coordination numbers with for Eu³⁺ ions. The ca. 1:1 ratio of Eu-Eu and Eu-Zn pairs, found for the temperature range 200-700 °C, points towards small clusters in the range of 4 to 8 Eu atoms, considering that edge and face sharing Eu(O₂)Zn and Eu(O₃)Zn bridges that could compensate for central Eu atoms being bridged only to Eu atoms, are highly unlikely for charge separation and bonding reasons. This fits the fact that even with a concentration as high as 5 at% of the strongly x-ray and electron scattering Eu atoms, there were no clear XRD peaks observed and no clusters easily detected in TEM imaging for the 600 °C sample being a pure oxide. These clusters should therefore be very small and aperiodic in nature. Another consequence is that with Eu-doping as high as 5% Eu, there should only be ca. 1-2 nm of ZnO between the Eu-clusters, when having an even distribution of Eu clusters in sizes small enough not to be observed with XRD or TEM. Based on the composition, each of the ca. 10 nm sized ZnO crystals should contain ca. 1100 Eu and 22000 Zn atoms. This corresponds ca. 150-300 Eu₈ or Eu₄ clusters, and implies that there is ca. 1-2 nm (3-4 ZnO₄ tetrahedra) of ZnO between the clusters, if evenly distributed. It can also be observed, in line with previous XRD, TEM and XPS studies,⁽⁴⁶⁾ that at temperatures from 700 °C, phase separation of the Eu-doped ZnO nanosponges into ZnO with low, or no Eu content and *c*-Eu₂O₃ took place. This, likely as a consequence of a metastable nature of the cluster structures.

3.3. DFT modelling of the ZnO:Eu structure

A few theoretical studies on Eu-doping in ZnO can be found in the literature.⁽⁶⁴⁻⁷⁰⁾ Yet, to the best of our knowledge, the possibility of Eu-oxide cluster formation, as observed here, has not been considered so far. Most of these theoretically calculated structures considered single atom doping,⁽⁶⁴⁻⁶⁸⁾ isovalent doping,^(69,70) or doping associated with point defects at Zn sites (substitutional). However, the much larger ionic radius (84 versus 60 pm) of 4-coordinated Eu³⁺ ions in the Zn²⁺-ion position in the *h*-ZnO host structure is far from optimal for Eu³⁺ ions as substitutional defects.

To gain insight into the ZnO:5%Eu structures, a series of theoretical total energy evaluations at a constant Eu-doping concentration corresponding to 4.17 at% Eu, with respect to the total number of metal-ions, were performed using DFT. In the evaluation, one Zn²⁺ vacancy per two Eu³⁺ ions was added to achieve charge neutrality. 23 cases of (Eu₂O₃)_x clusters with *x* = 1, 2, or 4, depending on super-cell size, all with the same overall doping concentration, were embedded in the host lattice were compared. A summary of the overall energetic and structural information in the form relative total energies for a representative set of Eu-doping configurations, are given in Figure 7. Structure 1, set as reference point for the cluster comparisons in Figure 7, represents a structure with the Eu³⁺ ions and the accompanied Zn²⁺-ion vacancies were randomly distributed, within the ZnO structure.

The first cluster structures, represented by structure 2, compared Eu^{3+} -dimer formation, i.e. $\text{Eu}^{3+}\text{-Zn}_{\text{vac.}}\text{-Eu}^{3+}$ clusters, is as previously discussed.⁽⁴⁸⁾ This step resulted in a huge energy gain of 1.06 eV per cluster. Structure 3 to 5 in Figure 7 show examples of further clustering with different cases of $(\text{Eu}^{3+}\text{-Zn}_{\text{vac.}}\text{-Eu}^{3+})_2$ clusters that were formed with 4 or 8 Eu atoms. As can be seen, further clustering is not as energetically favourable as the first $(\text{Eu}^{3+}\text{-Zn}_{\text{vac.}}\text{-Eu}^{3+})$, but still sizeable. The largest energy gain found in this study for $(\text{Eu}^{3+}\text{-Zn}_{\text{vac.}}\text{-Eu}^{3+})_2$ formation is 0.3 eV / $(\text{Eu}^{3+}\text{-Zn}_{\text{vac.}}\text{-Eu}^{3+})$ cluster.

The energy gain when forming the simplest $\text{Eu}^{3+}\text{-Zn}_{\text{vac.}}\text{-Eu}^{3+}$ cluster for a local charge neutrality is thus large, but the large ionic radius of the Eu^{3+} ion, even in its smallest four-coordination form should be hard to accommodate and align with the ZnO lattice, even if the Eu^{3+} ions can be displaced using the void of the Zn^{2+} vacancy. Therefore, there should be strain on the ZnO lattice reducing its stability compared to the larger Eu-oxide clusters involving 4-8 Eu^{3+} ions.

It thus seems that $(\text{Eu}_2\text{O}_3)_x$ clusters with $x = 2\text{-}4$ being similar in energy are optimal in providing a possibility to include the Eu^{3+} ions, while keeping the ZnO structure fairly intact. Here the ability for the Eu^{3+} ions, having a spherical outer orbital shell, makes it possible to adopt more or less any number of oxygen ligands, bond-lengths and spatial distribution of bonds, to achieve as suitable electronic saturation by ligand electron donation, as possible. This finding is supported by some tests with even higher x -values. A restriction in optimal size might stem from an optimal Lewis acid-base interaction between the ZnO and Eu_2O_3 where an overall electron donation from Eu_2O_3 to the ZnO is expected.

Comparison with experimental data. The ZnO:5%Eu sponge obtained at 600 °C showed no organic or carbonate residues, and nor any detectable phase separation, and is therefore the most intriguing and interesting to describe, and fits the pure non-phase-separated oxide DFT modelled here.

As discussed above, the EXAFS data indicated a close to unchanged ZnO lattice upon doping with the large, alio-valent Eu^{3+} ions forming small oxide-clusters within the ZnO crystals. The Eu^{3+} ions in these clusters were coordinated by a very unusual low average of ca. 5.1 oxygens, and showed a wide distribution of bond-lengths and directions. As shown above, the EXAFS data fitted well the XRD, TEM and XPS data where the TEM showed that the Eu-oxide clusters had to be small and non-periodical not to be easily observed and the XRD data showed an approximate increase in unit cell volume of ca. 0.4% for the 5%Eu doping.^(48,49)

This means that complementary, and in parts, much uncommon experimental results are present that can be used to verify the validity of theoretical DFT-based structural description of the Eu-cluster structures within the ZnO crystals.

Thus, the 23 theoretical structures including different Eu-cluster structures, and one un-doped ZnO structure (structure 20), could be judged not only by their relative energies (ΔE), but also on the experimentally obtained Eu-doped ZnO unit-cell volume relative to ZnO ($\Delta V\%$), Eu-to-oxide coordination number (CN), Eu-Eu distances ($d(\text{Eu-Eu})$ (Å)). Figure 8, gives these data arranged in total energy order for a comprehensive overview of these parameters.

Formation energy, coordination and ZnO:5%Eu unit cell volume. The structures ordered in relative energy (ΔE) start from structure 23, which represents a random distribution of Eu^{3+} ions and Zn^{2+} -vacancies which is 0.43 eV above the highest energy $(\text{Eu}_2\text{O}_3)_1$ cluster, 21, having paired Eu^{3+} ions flanking a Zn^{2+} vacancy. The clusters 13 to 21 have different spatial orientations of the $(\text{Eu}_2\text{O}_3)_1$ clusters within the ZnO structure. It can be seen that the ΔE for these clusters drop differ little. It can be noted that all these clusters, except the two with the lowest ΔE have Eu^{3+} ions with all CN 4. Similarly, the ZnO ΔV_{ZnO} is roughly 1.8%, for the CN4 based clusters, while the two lowest clusters in ΔE , 13 and 14, having average CN of 4.5 have, a lower ΔV_{ZnO} of 1.0-1.3%. It thus indicates, as expected, that it is hard to accommodate the large Eu^{3+} ions at positions close to the tetrahedral Zn^{2+} lattice positions, even when there is a metal vacancy nearby in small clusters. The size mismatch leads to an increased ZnO unit cell volume and high formation energy. Some relaxation in the ZnO structure can be seen in clusters containing higher Eu CN of 4.5 (structure 11) and 5 (structure 9) yielding ΔE comparable with the highest energy clusters with 4 and 8 Eu^{3+} ions. However, these clusters show very high ΔV_{ZnO} of 1.5-1.5%, not compatible with the experimental results.

Further clustering of $(\text{Eu}_2\text{O}_3)_1$ pairs to Eu4 and Eu8 clusters led to a distinct drop in formation energy by 0.30 eV. As for the $(\text{Eu}_2\text{O}_3)_1$ clusters, the $(\text{Eu}_2\text{O}_3)_x$ ($x = 2$ and 4) clusters with different spatial arrangements showed a range of formation energies from 1.03 eV below the reference structure, 22, to the three lowest values found for structure 0, 1 and 2 at 1.30-1.38 eV below the reference structure. This

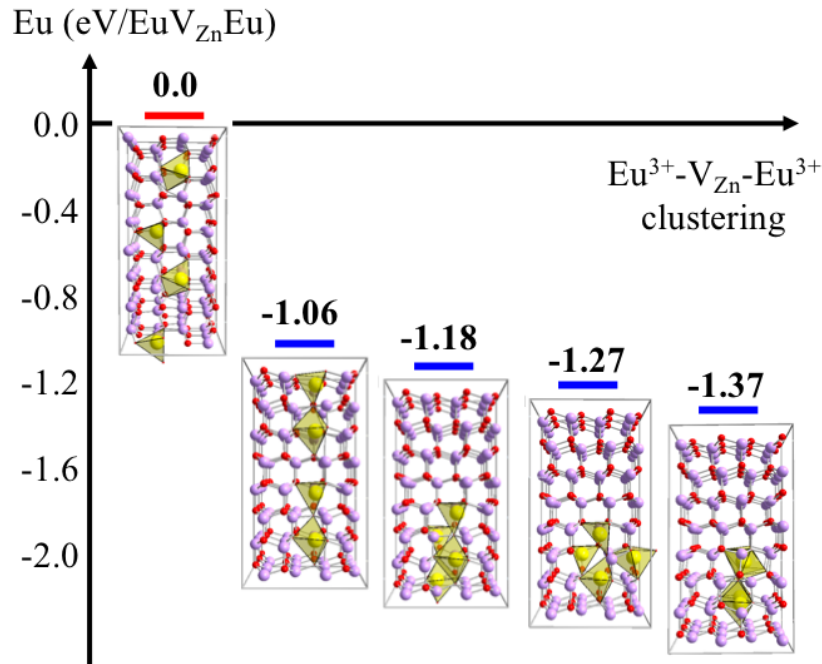


Figure 7. Relative formation energies of $(\text{Eu}^{3+}\text{-Zn}_{\text{vac.}}\text{-Eu}^{3+})$ structures with respect to a random distribution of Eu^{3+} ions and Zn^{2+} vacancies.

is a sizeable energy difference to the Eu4 and Eu8 clusters of up to 0.35 eV or ca. 30 kJmol⁻¹, although the difference to the reference structure which is similar to the sometimes discussed random Eu doping

in Zn-ion positions is very substantial with 1.38 eV, or 133 kJmol⁻¹. It can be observed that of the three lowest formation energies found for structure 0, 1 and, 2 the two first are Eu₄ clusters and the latter, an Eu₈ cluster. The other Eu₈ cluster analysed, structure 7, is found in the midst of the Eu₄ clusters, which indicates that the Eu₄ and 8 clusters are generally rather similar in ΔE and at clearly lower formation energies than smaller clusters. This also fits the fact that it has been hard to reveal the Eu-clusters with conventional HR TEM. These three clusters, are also the ones fitting the experimental data best with 0.58-0.68% ΔV_{ZnO} , compared to ca. 0.4% determined by XRD, and Eu CN of 4.87-4.94, compared to ca. 5.1 determined by EXAFS in this work. Such small volume changes and differences in average Eu CN are hard to determine experimentally, and the theory fits experimental data within a judged real error.

It can be observed that these three lowest energy clusters differ amongst the Eu₄ and Eu₈ clusters in having a higher Eu CN and higher ΔV_{ZnO} . It could be speculated that low Eu CN is hard to combine with the ZnO structure containing the much smaller Zn²⁺-ion and that a consequence of low CN is an increased ZnO unit cell volume.

Eu-Eu distances. Examples of coordination figures from the literature showing short to long Eu-Eu distances in oxides and related alkoxide structures are shown in [Figure 8](#). The *c*-Eu₂O₃ expelled from the ZnO:Eu crystals upon heating at higher temperatures have all six-coordinated Eu³⁺ ions and all four-coordinated oxygens.⁽⁵⁹⁾ The Eu-Eu distances in this structure are close to 3.60 Å. There also exists the high temperature polymorph *m*-Eu₂O₃ above 1200 °C, which has a mix of six- and seven-coordinated Eu³⁺ ions and a large variation of Eu coordination figures and Eu-Eu distances. The Eu-Eu distances in this oxide range from 3.33 to 5.49 Å, with the shortest distance found between Eu³⁺ ions in face sharing Eu(O₃)Eu pairs (3.33 Å) and the longest for strait Eu(O)Eu bonds, being 5.09 Å with CN 6 Eu³⁺ ions and 5.49 Å between CN 7 Eu³⁺ ions. Another example of close to linear (170 °) Eu-O-Eu bonds with CN 6 Eu³⁺ ions is found in the molecular Eu-oxo-alkoxide, Eu₅O(OPrⁱ)₁₃, which shows Eu-Eu distances of 4.82-4.87 Å.⁽⁷¹⁾ This molecule also contains close to 90° Eu-O-Eu angles in the base plane of this pyramidal molecule, which results in very short Eu-Eu distances of down to 3.42-3.43 Å. These distances set the expected minimum and maximum Eu-Eu distances expected for CN6 and CN7 Eu³⁺ ions in the present Eu-oxide clusters. For lower coordination numbers, even shorter distances could be considered, but the Eu³⁺-Eu³⁺ electronic repulsion should make it energetically costly to form.

It can be observed that the Eu-Eu distances in the 23 clusters studied are within reasonable minimum and maximum values, as discussed above. The Eu₈ cluster in structure 7, has an Eu-Eu distance that could be too short, although it is borderline, considering the possibility of lower Eu CN than in the literature examples.

The three lowest formation energy clusters show Eu-Eu distances in the range 3.42 to 4.75 Å, which are reasonable distances and fit the EXAFS data very well. These clusters are also small enough to have close to a 1:1 ratio of Eu-Eu and Eu-Zn pairs, as given by the EXAFS data. Considering the low

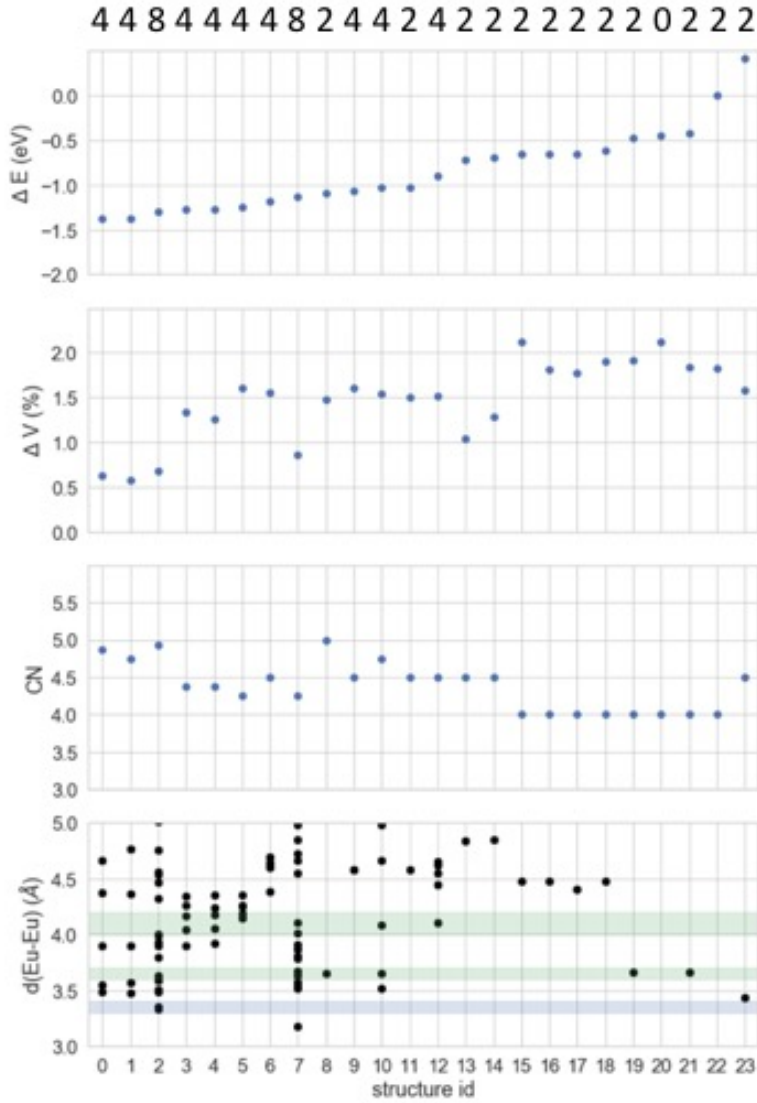


Figure 8. Theoretical structures of the composition ZnO:4.17%Eu with europium cluster compositions based on $(\text{Eu}_2\text{O}_3)_x$ pairs embedded in ZnO with $x = 1, 2$ and 4 . The structures are ordered in total formation energy per Eu_2O_3 cluster (ΔE , eV) relative to a random ordering of 2 Eu^{3+} -ions and one Zn^{2+} vacancy for charge neutralisation. The ZnO unit-cell volume change versus un-doped ZnO (ΔV , %), average Eu coordination number (CN) and Eu-Eu distances ($d(\text{Eu-Eu})$, Å) are also given for each structure. (Structure 20 is an undoped ZnO structure)

difference in energy between the Eu4 and Eu8 clusters, and the energy leap to the Eu2 clusters, it is not unlikely that there is a distribution of cluster sizes with even numbers of Eu atoms, in the range 4-8 Eu atoms. It is therefore interesting to study their structures in more detail.

Eu-oxide cluster structures. In Figure 9, examples of the low energy structures 0 and 2, with Eu4 and Eu8 clusters respectively, shown along with a structure containing Eu2 clusters. The latter

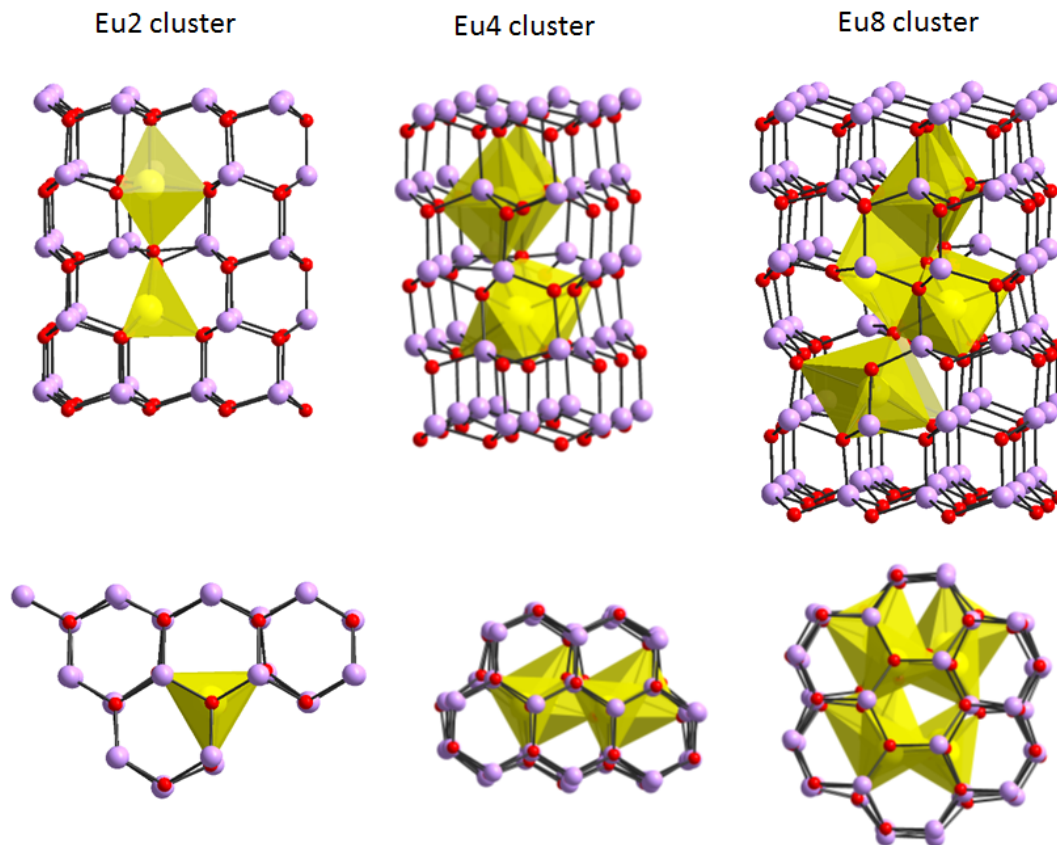


Figure 9. Structures of viewing the ZnO cell from (upper row) the a,b-direction and (lower row) down the c-direction: (left) a low energy Eu2 cluster with a CN of 4.5, (mid) a low energy Eu4 cluster and (right) an Eu8 cluster.

structure having the two Eu^{3+} ions aligned along the ZnO c-axis with an average Eu CN of 4.5 has a relatively low formation energy within the group of Eu2 containing ZnO structures.

It can be observed that in all cases, the Eu-oxide clusters are surrounded by an almost intact ZnO lattice. The cage structures, built from ZnO tetrahedra around the Eu-oxide clusters, are in some ways similar clathrates of water and inclusion compounds such as MOF's, enclosing larger atoms or molecules in a crystalline host. However, when looking closer there are some small distortions in the ZnO lattice close the clusters which causes the differences in ZnO unit cell volume and total formation energy of the Eu-doped ZnO structures. It was also be observed that all Zn-ions were tetrahedrally coordinated to oxygens bonded to other Zn or Eu^{3+} ions in a cluster. This indicates that lowering of the energy in these structures is dominated by providing the ZnO structure optimal coordination and distances. But, with all Eu^{3+} ions connecting to a Zn-ion, there is also close to optimal conditions for electronic donation from the Eu^{3+} ion coordinated Lewis basic oxygens to the more Lewis acidic Zn^{2+} -ions which should provide stabilisation.

At the connection between the Eu-oxide clusters and the host ZnO, there are no dangling bonds from unsaturated three-coordinated Zn tetrahedral found. Instead, there are Zn-O-Eu bonds with the Zn-

O tetrahedron rather intact in its typical coordination figure, as was also given experimentally by EXAFS.

There are some common features in how the lowest energy clusters of different sizes are embedded in the ZnO structure. From [Figure 9](#), it can be observed when viewing along the ZnO c-axis, the clusters prefer to be aligned along the c-axis and end with a trigonal bipyramidal Eu-ion, connecting to the Zn atom in the 0001 plane through at the apex, and to the 000-1 plane, via the triangular face of a tetrahedron or octahedron.

The Eu₂ clusters with the lowest formation energy are aligned along the ZnO c-axis with the Eu³⁺ ions making use of the Zn-ion vacancy volume to form a bond to the other Eu-ion creating a trigonal bipyramid in a suitable size to fit the ZnO structure, as well as a tetrahedron positioned to fit the ZnO structure through a trigonal face. This leaves an average Eu CN of 4.5 and allows the large Eu³⁺ ions to move closer to the vacancy volume and form a trigonal bipyramid with short equatorial Eu-O bonds and long axial bonds fitting the smaller ZnO structure. This differ from doping modes in structures with all tetrahedral Eu³⁺ ions which are higher in formation energy as can be observed in [Figure 8](#).

The Eu₄ and Eu₈ clusters have similar build-ups with Eu³⁺ ions coordinated by 4, 5, and 6 oxygens forming strongly distorted coordination polyhedra. This allows the Eu³⁺ ions flexibility in forming suitable bonds to the relatively stiff ZnO cage, while optimising the charge transfer between Eu³⁺ ions and oxygens within the cluster through highly distorted and varied Eu-oxygen polyhedral, allowed by the spherical outer shell. The wide range of coordination numbers, bond-lengths, and directions fit the broad peaks observed by EXAFS.

3.4. Optical properties

The Eu³⁺ ion is well-known for its excellent optical properties that can be leveraged into technological applications or be used to probe the dopant ion's local structural environment in a host lattice.⁽⁷²⁾ Therefore, the optical properties of the Eu-doped ZnO nanosponges were investigated by steady-state and time-resolved excitation, and emission spectroscopy. As representative samples, nanosponges obtained at 400, 600, and 800 °C were investigated. While the 400 °C sample, which contains residual carbonate,⁽⁴⁸⁾ was not studied by EXAFS, it is expected to exhibit similar Eu₄- to Eu₈-oxide clusters as observed by EXAFS for the 200 and 600 °C samples. As mentioned above, the 600 °C sample is of particular interest as it is free from organic or carbonate residues, while showing no detectable phase separation into ZnO and *c*-Eu₂O₃. In contrast, *c*-Eu₂O₃ was separated as secondary crystalline phase in the 800 °C sample.

[Figure 10a-c](#) shows excitation spectra monitoring the characteristic Eu³⁺ ⁵D₀ → ⁷F₂ *f-f* transition at 614 nm (in lighter colours) and the ZnO matrix emission at 545 or 550 nm (in darker colours). Irrespective the monitored emission and synthesis temperature, the recorded excitation spectra exhibit two regions of distinct spectral features, namely below and above 375 nm. At wavelengths shorter than 375 nm, a broad band arises at ca. 330 nm, the intensity of which strongly increases for higher temperatures of 600

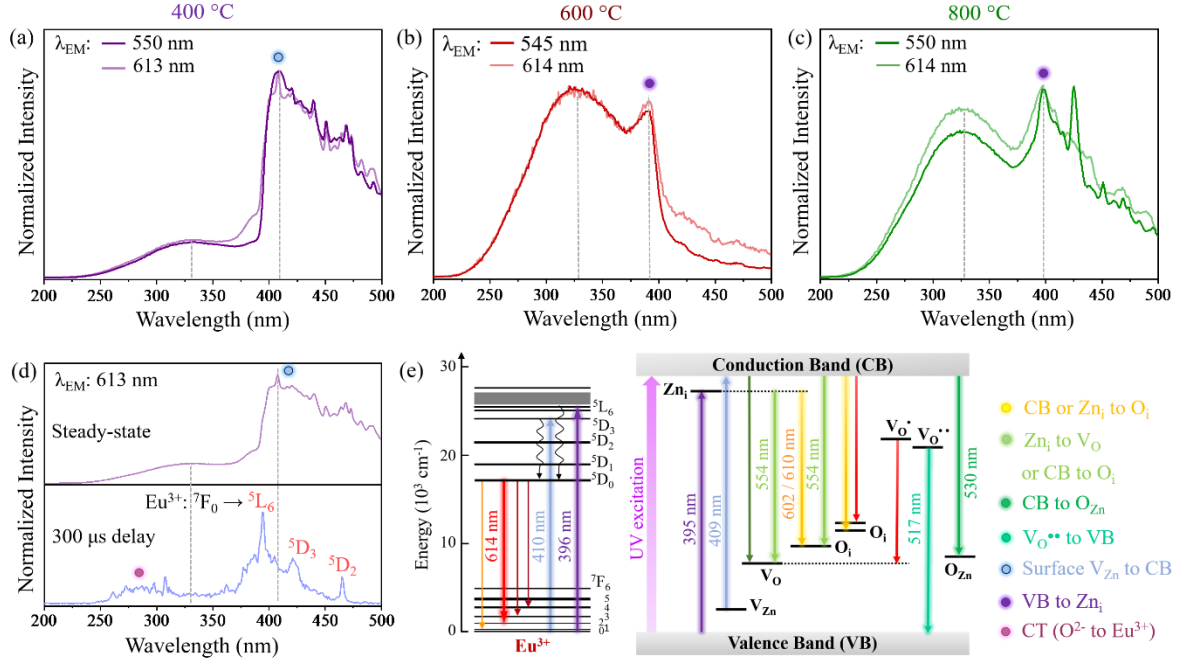


Figure 10. (a-c) Steady-state excitation spectra of ZnO:Eu nanosponges obtained at 400, 600, and 800 °C, respectively, showing different spectral profiles stemming from various ZnO defect types. (d) Bottom: Time-resolved excitation spectrum of the sample obtained at 400 °C, showing Eu³⁺ *f-f* excitation bands after a delay of 300 μs. Top: Steady-state spectrum added to highlight the contribution of ZnO excitation on the overall spectral features. (e) Energy level scheme showing the Eu³⁺ energy levels (left) (72) and ZnO defect levels (middle) in addition to valence (VB) and conduction band (CB) (O_{Zn}: anti-site oxygen atoms, V_{Zn}: zinc vacancies, V_O: oxygen vacancies, Zn_i: interstitial zinc atoms, O_i: interstitial oxygen atoms, V_O[•] and V_O^{••}: singly and doubly ionized oxygen vacancies, CT: charge transfer). The attribution of the main excitation (and emission, Figure 10, *vide infra*) bands is given on the right.

and 800 °C. Photons in the UV spectral region of the observed band have an energy high enough to excite an electron in the ZnO valence band (VB) to the conduction band (CB).

Analysing the spectral region above 375 nm, the excitation profile changed significantly between the 400 °C sample on the one side (Figure 10a) and the 600 and 800 °C samples on the other (Figure 10b,c). This variation in spectral features indicates the presence of different defect states lying in the band-gap of ZnO (Figure 10e). (49) The sample obtained at 400 °C exhibits an excitation band at 409 nm (Figure 10a), which can be ascribed to an absorption from the energy level attributed to zinc vacancies (V_{Zn}) at the crystal surface to the ZnO conduction band (Figure 10e). (73) Following excitation into the CB, radiative decay to defect states related to, for instance, oxygen vacancies (V_O), interstitial oxygen atoms (O_i) or anti-site oxygen atoms (O_{Zn}) can trigger the monitored green ZnO emission. Conversely, the excitation band at 409 nm was not observed for samples synthesised at 600 and 800 °C, respectively (Figures 10b,c). Instead, bands at 392 and 398 nm likely stemming from transitions between the ZnO valence band and interstitial zinc atoms (Zn_i) were observed in these samples. (73) Subsequent

radiative decay from Zn_i to V_O defect states is one possible pathway generating the monitored green ZnO emission. It is worth mentioning, that the precise assignment of the excitation and emission (*vide infra*) bands resulting from the different type of defects induced in the ZnO matrix is still under debate, and therefore the above attributions were suggested based on the literature and our previous spectroscopic observations for these materials.(49) Time-resolved excitation spectroscopy on the 400 °C sample allowed to suppress the detection of fast ZnO-related excitation bands to monitor the Eu^{3+} emission at 613 nm as a function of the excitation wavelength after a time delay. Figure 10d (bottom) shows several Eu^{3+} *f-f* excitation bands ascribed to the $^7F_0 \rightarrow ^5L_6$, $^7F_0 \rightarrow ^5D_2$, and $^7F_0 \rightarrow ^5D_3$ transitions. The lack of the weak excitation band at ca. 330 nm as well as the strong excitation band at 409 nm in the time-resolved spectrum (Figure 10d, bottom) versus their presence in the steady-state spectrum (Figure 10d, top) supports that both bands are ZnO-related. Besides the peaks ascribed to Eu^{3+} *f-f* transitions, an additional weak broad band was observed at ca. 280 nm. The origin of this excitation band is suggested to be a $Eu^{3+} \leftarrow O^{2-}$ charge transfer (CT), whereas oxygen in the Eu-oxide clusters, formed inside the ZnO matrix, can transfer energy to Eu^{3+} ions. These broad bands have been observed in other Eu-based oxides and been attributed to the overall combination of charge transfer transitions in metal–oxygen polyhedra.(74-77)

Based on the insights gained by excitation spectroscopy, emission spectra were recorded under excitation either into the ZnO conduction band or at specific ZnO defect levels, resulting in significantly different spectral profiles for samples obtained at 400, 600, and 800 °C (Figure 10a-c). For any of the three temperatures investigated, UV excitation at ca. 330 to 350 nm (darker colour curves) resulted in a broad band emission centred in the green spectral region. Green ZnO emission is often ascribed to oxygen deficiency (i.e., V_O or excess Zn^{2+} ions).(78) Yet, it has also been related to interstitial (O_i) and anti-site (O_{Zn}) oxygen, as it may be induced upon thermal treatment of the ZnO nanosponges in air.(79,80) This may explain the slight blue-shift of the broad emission band for the 600 and 800 °C samples, respectively, compared to the 400 °C sample under excitation into the ZnO conduction band.

The sample obtained at 400 °C (Figure 11a) exhibited an additional sharp peak at 614 nm due to the main Eu^{3+} emission ($^5D_0 \rightarrow ^7F_2$) (72), not present for the other samples. Changing the excitation wavelength to match the most intense excitation band for ZnO defect levels in the 400 °C sample, i.e., 409 nm (surface V_{Zn} to conduction band, lighter colour curve), sharp emission bands due to ZnO defect states – including oxygen-related defect states in the 500 to 600 nm spectral range – in addition to the $^5D_0 \rightarrow ^7F_2$ Eu^{3+} emission were observed (Figure 11a). Time-resolved emission spectroscopy of the Eu^{3+} emission under 409 nm excitation (Figure 11d, bottom) further confirmed the characteristic Eu^{3+} emission bands, whereas suppression of the ZnO emission clearly unveiled the emission bands characteristic for the Eu^{3+} $^5D_0 \rightarrow ^7F_J$ ($J = 0, 1, 2, 3$, and 4) transitions. The lack of spectral fine-structure in these bands can be caused by structural disorder (81) around the Eu ions, induced by, for instance, carbonate residues, ZnO-related defects and Eu-oxide clusters that are expected to be formed (e.g., at

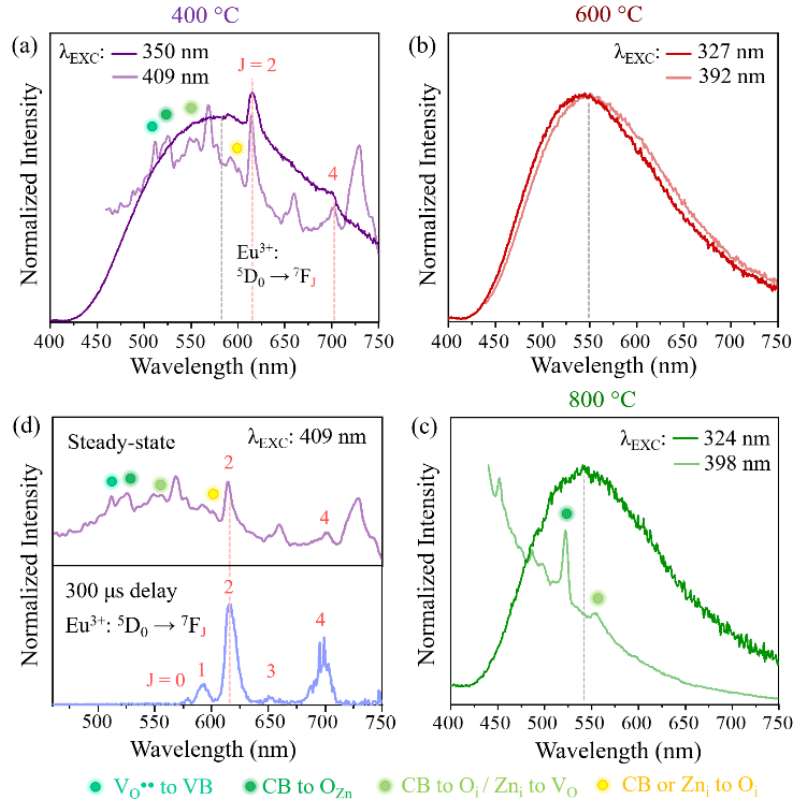


Figure 11. (a-c) Steady-state emission spectra of ZnO:Eu nanosponges obtained at 400, 600, and 800 °C, respectively, showing different spectral profiles stemming from various ZnO defect types. (d) Bottom: Time-resolved emission spectrum of the sample obtained at 400 °C, showing Eu^{3+} emission bands after a delay of 300 μs . Top: Steady-state spectrum added to highlight the contribution of ZnO emission on the overall spectral features.

200 and 600°C). Generally speaking, under UV illumination, direct excitation of Eu^{3+} ions into the $^5\text{D}_1$ excited states is possible. Yet, due to the small absorption cross-section of Eu^{3+} compared to ZnO, this direct excitation pathway can most likely be considered negligible. In addition, the radiative and non-radiative decay of excitons in ZnO is much faster ($> 10^2$ times) when compared to energy transfer rates to Eu^{3+} , which hinders the direct ZnO (conduction band)-to- Eu^{3+} energy transfer, but could lead to an emission-reabsorption mechanism. (82) Consequently, defect states in the ZnO host are key to mediate energy transfer to the higher-laying Eu^{3+} levels (e.g. $^5\text{L}_6$ or $^5\text{D}_3$). Subsequent non-radiative decay to the emitting $^5\text{D}_0$ level is followed by radiative decay down to the $^7\text{F}_J$ levels giving rise to the characteristic red Eu^{3+} emission (Figure 10e, left scheme). (83-85)

In contrast to the 400 °C sample, the samples obtained at 600 and 800°C – free from carbonate or other organic residues, but containing Eu-oxide clusters similar to those in the 400 °C sample and additional $c\text{-Eu}_2\text{O}_3$ in case of 800 °C – exhibited only emission bands assigned to the ZnO matrix, regardless the excitation wavelength used to acquire the emission spectra (Figure 11b,c). In order to ensure that the broad ZnO emission does not overlap any underlying Eu^{3+} emission, additional time-

resolved emission spectroscopy was performed on the 600 and 800 °C samples. However, no emission was observed under any of the ZnO defect- or Eu^{3+} -related excitation wavelengths tested (namely, 330, 409, 392, 398, 464 nm – data not shown). In our previous study on Eu-doped ZnO nanosponges,⁽⁴⁹⁾ similar severe quenching of the Eu emission was observed for samples obtained at temperatures above 400 °C, which was attributed to two possible aspects: (1) the presence of phase separation into ZnO and *c*- Eu_2O_3 at higher annealing temperatures inducing concentration quenching; and (2) the increased number of oxygen-related defect levels induced by heating in air at elevated temperatures, resulting in less efficient energy transfer from ZnO defect states to Eu due to the energy mismatch between these oxygen-related energy levels and the Eu excited levels (Figure 10e). Here obtained excitation spectra provide additional insight into the ZnO defect structure, not available in our previous study (Figure 10b, c). Samples annealed at 600 and 800 °C exhibited a peak at ca. 395 nm, which can be ascribed to Zn_i related defects in the ZnO matrix. The high-lying energy level of this defect type provides a good energy match with the Eu^{3+} excited states (Figure 10e), potentially enabling ZnO-to-Eu energy transfer. Hence, possible energy transfer from ZnO to Eu should not be ruled out, even when higher synthesis temperatures were applied. However, as complete lack of subsequent Eu^{3+} emission was demonstrated by time-resolved emission spectroscopy, some quenching mechanism must take place. In lanthanide-doped materials, photoluminescence quenching can be caused when the average distance between the luminescent centres is lower than a critical distance, known as concentration or self-quenching. For Eu^{3+} , a critical distance of less than 5 Å is commonly considered as close enough for the exchange interaction mechanism of energy transfer to become operative.^(72,86) As demonstrated by EXAFS and DFT studies, the Eu-Eu distances in the formed Eu-oxide clusters (600 °C) are well within this critical range, hence, their contribution to Eu^{3+} luminescence quenching cannot be ruled out. Moreover, the formation of *c*- Eu_2O_3 particles in the 800 °C sample is expected to foster non-radiative energy transfer among the luminescent Eu^{3+} centres. While self-quenching is a plausible explanation for the observed loss of Eu^{3+} emission, the emission spectrum of the 800 °C sample can provide additional insight (Figure 11c): the two bands at 522 and 555 nm can be ascribed to a transition from the ZnO conduction band to O_{Zn} -type defects, as well as to transitions between energy levels related to Zn_i and V_O defects. Specifically, the Zn_i defect states are resonant with the excited $\text{Eu}^{3+} {}^5\text{L}_6$ level, offering a pathway for ZnO (Zn_i) \rightarrow $\text{Eu}^{3+} ({}^5\text{L}_6)$ energy transfer. Yet, as no Eu^{3+} emission was detected, such energy transfer may compete with the ZnO matrix-related radiative decay. If the latter is favoured, ZnO-to-Eu energy transfer would be hampered, which ultimately can explain the observation of green ZnO emission only.

Overall, the observed excitation and emission spectra of ZnO:Eu obtained at different temperatures show how the optical properties in ZnO:Eu nanosponges are strongly dictated by changes in the local host structure and the dopant ion environment, offering insight into structure-property relationships that are complementary to those found by EXAFS, DFT, XRD, and TEM techniques.

4. Conclusions

The mystery of how large amounts of large, alio-valent Ln^{3+} -ions can be introduced into the ZnO lattice without forming detectable extra phases and virtually no increase in unit cell volume for oxides heated at up to 600-900 °C, has been revealed. In these studies, XRD and TEM showed that for a ZnO:5%Eu doping in the nano-crystalline sponges, phase separation into ZnO with lower amount of Eu doping and $c\text{-Eu}_2\text{O}_3$ took place from 700 °C. XRD showed only a very small ZnO unit cell volume expansion of ca. 0.4 vol% on doping with the larger Eu^{3+} ions. The Zn K edge and Eu- L_3 edge EXAFS provided detailed information on the local bonding conditions which revealed an almost intact ZnO lattice, in line with the XRD studies, as well as very low Eu to O coordination numbers close to 5 for the non-phase separated 200 and 600 °C samples. The experimental data were compared with the formation energy, Eu coordination number, Eu-Eu distances, and ZnO unit cell volume expansion on Eu doping, for 23 DFT generated clusters. Very good agreement was obtained with respect to the given properties for 4-8 Eu atom containing clusters which indicated that these structures closely represent the real structure. This is thus a much unexpected dopant structure with magnetically and optically active molecule-like Eu-oxide clusters, embedded in an almost intact large band-gap semiconductor oxide, with a stability in air up to temperatures of several hundred degrees, depending on doping and Ln ion. This is exiting as it provides a foundation for combining molecular magnets and semi-conductors, which would make the sensitivity of the latter somewhat relaxed.

ASSOCIATED CONTENT

Supporting Information

Details of EXAFS data reduction, Error analysis

AUTHOR INFORMATION

Corresponding Authors

- * soham.mukherjee@physics.uu.se, soham.chem@gmail.com
- * hakan.rensmo@physics.uu.se
- * Gunnar.Westin@kemi.uu.se

Present Addresses

£

1

Notes

The authors declare no competing financial interest.

ACKNOWLEDGMENT

The authors acknowledge STandUP for Energy, the Swedish Research Council (Grant nos. VR 2018-06465, and 2018-04330), the Swedish Foundation for Strategic Research (Project no. RMA15-0130), the Swedish Energy Agency (Grant no. P43549-1) for financial support. E. H. and E. M. R. gratefully acknowledge the financial support provided by the University of Ottawa, the Canadian Foundation for Innovation (CFI), and the Natural Sciences and Engineering Research Council of Canada (NSERC). MRCAT operations are supported by the Department of Energy and the MRCAT member institutions. This research used resources of the Advanced Photon Source, a U.S. Department of Energy (DOE) Office of Science User Facility operated for the DOE Office of Science by Argonne National Laboratory under Contract No. DE-AC02-06CH11357. Support for author CUS was provided in part by the National Science Foundation under Grant No. DMR-086935.

REFERENCES

- (1) Özgür, Ü.; Alivov, Ya. I.; Liu C.; Teke, A.; Reshchikov, M. A.; Doğan, S.; Avrutin, V.; Cho, S.-J.; Morkoç, H. A comprehensive review of ZnO materials and devices. *J. Appl. Phys.* **2005**, 98, 041301, 1-103.
- (2) Kołodziejczak-Radzimska, A.; Jesionowski, T. Zinc Oxide—From Synthesis to Application: A Review. *Materials* **2014**, 7, 2833-2881.
- (3) Wang, Z. L. Zinc oxide nanostructures: growth, properties and applications. *J. Phys. Condens. Matter.* **2004**, 16, R829–R858.
- (4) Kharisov, B. I.; Kharissova, O. V.; García, B. O.; Méndez, Y. P.; Gómez, de la Fuente I. State of the art of nanoforest structures and their applications. *RSC Adv.* **2015**, 5, 105507–105523.
- (5) Cauda, V.; Pugliese, D.; Garino, N.; Sacco, A.; Bianco, S.; Bella, F.; Lamberti, A.; Gerbaldi, C. Multi-functional energy conversion and storage electrodes using flower-like Zinc oxide nanostructures. *Energy.* **2014**, 65, 639–646.
- (6) Hosono, E.; Fujihara, S.; Honma, I.; Zhou, H. The fabrication of an upright-standing zinc oxide nanosheet for use in dye-sensitized solar cells. *Adv. Mater.* **2005**, 17, 2091-2094.
- (7) Law, M.; Greene, L. E.; Johnson, J. C.; Saykally, R.; Yang, P. Nanowire dye-sensitized solar cells. *Nature Mater.* **2005**, 4, 455–459.
- (8) Anta, J. A.; Guillén, E.; Tena-Zaera, R. ZnO-Based Dye-Sensitized Solar Cells. *J. Phys. Chem. C* **2012**, 116 (21), 11413–11425.
- (9) Gonzalez-Valls, I.; Lira-Cantu, M. Vertically-aligned nanostructures of ZnO for excitonic solar cells: a review. *Energy Environ. Sci.* **2009**, 2, 19–34.
- (10) Selopal, G.S.; Wu, H.-P.; Lu, J.; Chang, Y.-C.; Wang, M.; Vomiero, A.; Concina, I.; Diau, E. W.-G. Metal-free organic dyes for TiO₂ and ZnO dye-sensitized solar cells. *Sci. Reports* **2016**, 6, 18756.
- (11) Zhang, Y.; Ram, M. K.; Stefanakos, E. K.; Goswami, D. Y. Synthesis, Characterization, and Applications of ZnO Nanowires. *J. Nanomater.* **2012**, 624520, 1–22.
- (12) Kumar, S.G.; Kavitha, R., Lanthanide ions doped ZnO based photocatalysts, *Separation, Purification Technol.* **2021**, 274, 118853, 1-33.
- (13) Lee, K. M.; Lai, C. W.; Ngai, K. S.; Juan, J. C. Recent developments of zinc oxide based photocatalyst in water treatment technology: A review. *Water Research* **2016**, 88, 428–448.
- (14) Boppella, R.; Anjaneyulu, K.; Basak, P.; Manorama, S. V. Facile Synthesis of Face Oriented ZnO Crystals: Tunable Polar Facets and Shape Induced Enhanced Photocatalytic Performance. *J. Phys. Chem. C* **2013**, 117(9), 4597–4605.
- (15) Liu, C.; Yun, F.; Morkoç, H. Ferromagnetism of ZnO and GaN: A review. *J. Mater. Sci. Mater. Electronics* **2005**, 16, 555-597.
- (16) Pearton, S. J.; Heo, W. H.; Ivill, M.; Norton, D. P.; Steiner T. *Dilute Magnetic Semicond. Oxides Semicond. Sci. Technol.* **2004**, 19, R59-R94.

- (17) Kittilstved, K. R.; Liu, W. K.; Gamelin, D. R. Electronic Structure Origins of Polarity Dependent High- T_C Ferromagnetism in Oxide Diluted Magnetic Semiconductors. *Nature Materials*, **2006**, *5*, 291–297.
- (18) Willander, M.; Nur, O.; Zhao, Q. X.; Yang, L. L.; Lorenz, M.; Cao, B. Q.; Pérez, J. Z.; Czekalla, C.; Zimmermann, G.; Grundmann, M. Zinc oxide nanorod based photonic devices: recent progress in growth, light emitting diodes and lasers. *Nanotechnol.* **2009**, *20*, 332001, 1–40.
- (19) Shi, L.; Cui, J.; Zhao, F.; Wang, D.; Xie, T.; Lin Y. High-performance formaldehyde gas-sensors based on three dimensional center-hollow ZnO. *Phys. Chem. Chem. Phys.* **2015**, *17*, 31316–31323.
- (20) Hoffmann, W. G.; Gad, A. E.; Prades, J. D.; Hernandez-Ramirez, F.; Fiz, R.; Shen, H.; Mathur, S. Solar diode sensor: Sensing mechanism and applications *Nano Energy* **2013**, *2*, 514–522.
- (21) Choi, K. J.; Jang, H. W. One-Dimensional Oxide Nanostructures as Gas-Sensing Materials: Review and Issues. *Sensors* **2010**, *10*, 4083–4099.
- (22) Zhang, J.; Wang, S.; Xu, M.; Wan, Y.; Zhu, B.; Zhang, S.; Huang, W.; Wu, S. Hierarchically porous architectures for gas sensor application *Cryst. Growth Design* **2009**, *9*, 3532–3537.
- (23) Behrens, M.; Robert, Schlögl, R. How to prepare a good Cu/ZnO catalyst or the role of solid state chemistry for the synthesis of nanostructured catalysts. *Z. Anorg. Allg. Chem.* **2013**, *639*, 2683–2695.
- (24) Hosseini-Sarvari, M. *Catal. Organic Reactions on ZnO. Current Org. Synth.* **2013**, *10*(5), 697–723.
- (25) Martínez-Suárez, L.; Siemer, N.; Frenzel, J.; Marx, D. Reaction Network of Methanol Synthesis over Cu/ZnO Nanocatalysts. *ACS Catal.* **2015**, *5*(7), 4201–4218.
- (26) Polshettiwar, V.; Baruwati, B.; Varma, R. S. Self-assembly of metal oxides into three-dimensional nanostructures: synthesis and application in catalysis. *ACS Nano* **2009**, *3*(3), 728–736.
- (27) Behrens, M.; Kasatkin, F. S.; Hävecker, S. K. M.; Abild-Pedersen, F.; Zander, S.; Girgsdies, F.; Kurr, P.; Knief, B.-L.; Tovar, M.; Fischer, R. W.; Nørskov, J. K.; Schlögl, R. The active site of methanol synthesis over Cu/ZnO/Al₂O₃ industrial catalysts. *Science* **2012**, *336*(6083), 893–897.
- (28) Caramia, V.; Bozzini, B. Materials science aspects of zinc–air batteries: a review. *Mater. Renew. Sustain. Energy* **2014**, *3*, 28, 1–12.
- (29) Parker, J. F.; Nelson, E. S.; Wattendorf, M. D.; Hevrin, C. N.; Long, J. W.; Rolison, D. R. Retaining the 3D framework of zinc sponge anodes upon deep discharge in Zn-air cells. *Appl. Mater. Interfaces* **2014**, *6*, 19471–19476.
- (30) Garino, N.; Lamberti, A.; Gazia, R.; Chiodoni, A.; Gerbaldi, C. Cycling behavior of sponge-like nanostructured ZnO as thin film Li-ion battery anodes. *J. Alloys Compd.* **2014**, *15*, S454–S458.
- (31) Mukherjee, S.; Phuyal, D.; Segre, C. U.; Das, S.; Karis, O.; Edvinsson, T.; Rensmo, H. Structure and Electronic Effects from Mn and Nb Co-doping for Low Band Gap BaTiO₃ Ferroelectrics. *J. Phys. Chem. C* **2021**, *125* (27), 14910–14923.
- (32) Ganegoda, H.; Mukherjee, S.; Ma, B.; Olive, D. T.; McNeely, J. H.; Kaduk, J. A.; Terry, J.; Rensmo, H.; Segre, C. U. Role of Fe Doping on Local Structure and Electrical and Magnetic Properties of PbTiO₃ *J. Phys. Chem. C* **2021**, *125*(22), 12342–12354.
- (33) Mukherjee, S.; Ganegoda, H.; Kumar, A.; Pal, S.; Segre, C. U.; Sarma, D. D. Evolution of the Local Structure within Chromophoric Mn–O₅ Trigonal Bipyramids in YMn_{1-x}In_xO₃ with Composition. *Inorg. Chem.* **2018**, *57* (15), 9012–9019.
- (34) Khan, A. H.; Dalui, A.; Mukherjee, S.; Segre, C. U.; Sarma, D. D.; Acharya, S. Efficient Solid-State Light-Emitting CuCdS Nanocrystals Synthesized in Air. *Angew. Chem. Int. Ed.* **2015** *54* (9), 2643–2648.
- (35) Dietl, T.; Ohno, H.; Cibert, J.; Ferrand, D. Zener model description of ferromagnetism in zinc-blende magnetic semiconductors, *Science*, **2000**, *287*, 1019–1022.
- (36) Ramachandran, S.; Tiwari, A.; Narayan, Zn_{0.9}Co_{0.1}-based diluted magnetic semiconducting thin films. *J. Appl. Phys. Lett.* **2004**, *84*, 5255–5257.
- (37) Yadav, A. K.; Maidul Haque, S.; Shukla, D.; Phase, D. M.; Jha, S. N.; Bhattacharyya, D. Defect mediated reversible ferromagnetism in Co and Mn doped zinc oxide epitaxial films. *J. Appl. Phys.* **2012**, *112*, 113917, 1–3.
- (38) Mal, S.; Nori, S.; Mula, S.; Narayan, J.; Prater, J.T. Defect mediated reversible ferromagnetism in Co and Mn doped zinc oxide. *J. Appl. Phys.* **2012**, *112*, 113917, 1–6.
- (39) White, M. A.; Lovejoy, T. C.; Ochsenbein, S. T.; Olmstead, M. A.; Gamelin, D. R. Sputtering Induced Co⁰ Formation in X-Ray Photoelectron Spectroscopy of Nanocrystalline Zn_{1-x}Co_xO Spinodal Enrichment Models. *J. Appl. Phys.*, **2010**, *107*, 103917.

- (40) Park, C. I.; Jin, Z.; Jeong, E.-S.; Hwang, I. H.; Han, S.W. Local structural properties of Co-ion-implanted ZnO nanorods *J. Korean Phys. Soc.* **2013**, 63, 2165–2169.
- (41) Sanyal, B.; Grånäs, O.; Knut, R.; Coleman, V. A.; Thunström, P.; Iuşan, D. M.; Karis, O.; Eriksson, O.; Westin, G. Electronic structure of Co doped ZnO: Theory and experiment. *J. Appl. Phys.* **2008**, 103, 07D130, 1-3.
- (42) Iuşan, D.; Knut, R.; Sanyal, B.; Karis, O.; Eriksson, O.; Coleman, V. A.; Westin, G.; Wikberg, J. M.; Svedlindh, P. Electronic structure and chemical and magnetic interactions in ZnO doped with Co and Al: Experiments and ab initio density-functional calculations. *Phys. Rev.* **2008**, B 78, 085319, 1-9.
- (43) Knut, R.; Wikberg, J. M.; Lashgari, K.; Coleman, V. A.; Westin, G.; Svedlindh, P.; Karis, O. Magnetic and electronic characterization of highly Co-doped ZnO: An annealing study at the solubility limit. *Phys. Rev. B* **2010**, 82, 094438, 1-7.
- (44) Kronawitter, C. X.; Zegkinoglou, I.; Shen, S.-H.; Liao, P.; Cho, I. S.; Zandi, O.; Liu, Y.-S.; Lashgari, K.; Westin, G.; Guo, J.-H.; Himpsel, F. J.; Carter, E. A.; Zheng, X. L.; Hamann, T. W.; Koel, B. E.; Mao, S. S.; Vayssieres, L. Titanium incorporation into hematite photoelectrodes: theoretical considerations and experimental observations. *Energy Environ. Sci.*, **2014**, 7, 3100-3121.
- (45) Marin, R.; Jaque, D. Doping lanthanide ions in colloidal semiconductor nanocrystals for brighter luminescence. *Chem. Rev.* **2021**, 121, 1425-1462.
- (46) Kumar, V.; Ntwaebrowa, O. M.; Soga, T.; Dutta, V.; Swart, H.C. rare earth doped zinc oxide nanophosphor powder: A future material for solid state lighting and solar cells. *Photonics*. **2017**, 4, 2613-2637.
- (47) Girish Kumar, S.; Kavitha, R. Lanthanide ions doped ZnO based photocatalysts. *Separation, Purif. Technol.* **2021**, 274, 118853, 1-33.
- (48) Katea, S. N.; Broqvist, P.; Kullgren, J.; Hemmer, E.; Westin, G. Fast, Low-Cost Synthesis of ZnO:Eu Nanosponges and the Nature of Ln Doping in ZnO. *Inorg. Chem.* **2020**, 59, 7584–7602.
- (49) Marin, R.; Oussta, F.; Naim Katea, S. Prabhudev, S.; Botton, G. A.; Westin, G.; Hemmer E. Europium-doped ZnO Nanosponges – Controlling Optical Properties and Photocatalytic Activity. *J. Mater. Chem. C*. **2019**, 7, 3909-3919.
- (50) Perdew, J. P.; Burke, K.; Ernzerhof, M. Generalized gradient approximation made simple. *Phys. Rev. Lett.* **1996**, 77, 3865-3868.
- (51) Perdew, J. P.; Burke, K.; Ernzerhof, M. Generalized gradient approximation made simple. *Phys. Rev. Lett.* **1996**, 78, 1396.
- (52) Kresse, G.; Hafner, J. Ab initio molecular dynamics for liquid metals. *Phys. Rev. B* **1993**, 47, 558–561.
- (53) Kresse, G.; Hafner, J. Ab initio molecular-dynamics simulation of the liquid-metal–amorphous-semiconductor transition in germanium. *Phys. Rev. B*, **1994**, 49, 14251–14269.
- (54) Kresse, G.; Furthmüller, J. Efficiency of ab-initio total energy calculations for metals and semiconductors using a plane-wave basis set. *Comput. Mater. Sci.* **1996**, 6(1), 15–50.
- (55) Kresse, G.; Furthmüller, J. Efficient iterative schemes for ab initio total-energy calculations using a plane-wave basis set. *Phys. Rev. B* **1996**, 54, 11169–11186.
- (56) Blöchl, P. E. Projector augmented-wave method. *Phys. Rev. B* **1994**, 50, 7953–17979.
- (57) Kresse, G.; Joubert, D. From ultrasoft pseudopotentials to the projector augmented-wave method. *Phys. Rev. B* **1999**, 59, 1758–1775.
- (58) Katea, S. N.; Hajduk, Š.; Crnjak Orel, Z.; Westin, G. Low Cost, Fast Solution Synthesis of 3D Framework ZnO Nanosponges. *Inorg. Chem.* **2017**, 56, 15150–15158.
- (59) Shannon, R.D. Revised effective ionic radii and systematic studies of interatomic distances in halides and chalcogenides. *Acta Cryst.* **1976**, A32, 751-767.
- (60) Zhang, Y.; Liu, Y.; Wu, L.; Xie, E.; Chen, J. Photoluminescence and ZnO → Eu³⁺ energy transfer in Eu³⁺-doped ZnO nanospheres. *J. Phys. D: Appl. Phys.* **2009**, 42, 085106.
- (61) Samah M. Ahmed Paul Szymanski, Lotfia M. El-Nadi, Mostafa A. El-Sayed, Energy-Transfer Efficiency in Eu-Doped ZnO Thin Films: The Effects of Oxidative Annealing on the Dynamics and the Intermediate Defect States, *ACS Applied Materials & Interfaces* **2014**, 6, 3, 1765-1772.
- (62) Yang, Y. H.; Feng, Y.; Zhu, H. G.; Yang, G. W. Growth, structure, and cathode luminescence of Eu-doped ZnO nanowires prepared by high-temperature and high-pressure pulsed-laser deposition. *J. Appl. Phys.* **2010**, 107, 053502.

- (63) Zhong W.-W.; Guan, G.-W.; Liu, X.-L.; Zhang, Li.; Liu, Y.-P.; Li, Z.-G.; Chen, W.-P. J. Effect of annealing on the structure and photoluminescence of Eu-doped ZnO nanorod ordered array thin films *Nanomater.* **2012**, 263679, 1-6.
- (64) Sebastian Geburt, Michael Lorke, Andreia L. da Rosa, Thomas Frauenheim, Robert Röder, Tobias Voss, Uwe Kaiser, Wolfram Heimbrod, and Carsten Ronning, Intense Intrashell Luminescence of Eu-Doped Single ZnO Nanowires at Room Temperature by Implantation Created Eu–O_i Complexes. *Nano Lett.* **2014**, 14, 4523–4528
- (65) Assadi, M. H. N.; Zhang, Y.; Zheng, R.-K.; Ringer, S. P.; Li, S. Structural and electronic properties of Eu- and Pd-doped ZnO. *Nanoscale Research Lett.* **2011**, 6:357
- (66) El Hachimi, A.G.; Ould NE, M.L.; El Yousfi, A.; Benyoussef, A.; El Kenz, A. Enhancing optical absorption in visible light of ZnO co-doped with europium and promethium by first-principles study through modified Becke and Johnson potential scheme, *J. Rare Earths*, **2019**, 37, 416-421.
- (67) Lorke, M.; Frauenheim, T.; da Rosa, A. L. Many-body electronic structure calculations of Eu-doped ZnO. *Phys. Rev.* **2016**, B 93, 115132.
- (68) Zhang, X.J.; Mi, W.B.; Wang, X.C.; Bai, H.L. First-principles prediction of electronic structure and magnetic ordering of rare-earth metals doped ZnO. *J. Alloys Compd.* **2014**, 617, 828-833.
- (69) Yumak, A.; Yahsi, U.; Petkova, P.; Boubake, K. Europium doping-induced stability and quantum confinement effect in ZnO quantum well wires QWW: Electronic structure calculation and material structural investigation in terms of band-gap shift. *Materials Letters* **2016**, 164, 89-92.
- (70) Yu, Q.; Ai, T.; Jiang, L.; Zhang, Y.; Li, C.; Yuan, X. Efficient energy transfer in Eu-doped ZnO on diamond film. *RSC Adv.* **2014**, 4, 53946 53949.
- (71) Westin, G.; Moustiakimov, M.; Kritikos, M. Synthesis, Characterization, and Properties of Three Europium 2-Propoxides: [Eu₄(OPrⁱ)₁₀(HOPrⁱ)₃] 2HOPrⁱ, Eu₅O(OPrⁱ)₁₃, and EuAl₃(OPrⁱ)₁₂. *Inorg. Chem.* **2002**, 41, 3249–3258.
- (72) Binnemans, K. interpretation of europium (III) spectra. *Coord. Chem. Rev.* **2015**, 295, 1-45.
- (73) Chen, D.; Wang, Z.; Ren, T.; Ding, H.; Yao, W.; Zong, R.; Zhu, Y. Influence of Defects on the Photocatalytic Activity of ZnO. *J. Phys. Chem. C* **2014**, 118, 15300-15307.
- (74) Ran, W.; Noh, H. M.; Park, S. H.; Moon, B. K.; Jeong, J. H.; Kim, J. H., Shi, J. *Scientific Reports*, **2018**, 8, 5936.
- (75) Yang, L.; She, Y.; Zhao, S.; Yue, S.; Wang, Q.; Hu, A.; Zhang, W. Synthesis and optical properties modulation of ZnO/Eu₂O₃ nanocable arrays. *J. Appl. Phys.* **2010**, 108, 104301.
- (76) Wakefield, G.; Keron, H. A.; Dobson, P. J.; Hutchison, J. H. Synthesis and Properties of Sub-50-nm Europium Oxide Nanoparticles. *J. Colloid Interface Sci.* **1999**, 215, 179–182
- (77) Roof, I. P.; Smith, M. D.; Park, S.; zur Loye, H.-C. EuKNaTaO₅: Crystal Growth, Structure and Photoluminescence Property *J. Am. Chem. Soc.* **2009**, 131, 4202–4203.
- (78) Zheng, Y.; Chen, C.; Zhan, Y.; Lin, X.; Zheng, Q.; Wei, K.; Zhu, J.; Zhu, Y. Luminescence and Photocatalytic Activity of ZnO Nanocrystals: Correlation between Structure and Property. *Inorg. Chem.* **2007**, 46, 6675–6682
- (79) Can, M. M.; Shah, S. I.; Doty, M. F.; Haughn, C. R.; Firat, T. Electrical and optical properties of point defects in ZnO thin films. *J. Phys. D: Appl. Phys.* **2012**, 45, 195104.
- (80) Raji, R.; Gopchandran, K. G. ZnO nanostructures with tunable visible luminescence: Effects of kinetics of chemical reduction and annealing. *J. Sci.: Adv. Mater. Dev.* **2017**, 2, 51-58.
- (81) Jang, K. W.; Meltzer, R. S. Homogeneous and inhomogeneous linewidths of Eu³⁺ in disordered crystalline systems *Phys. Rev. B* **1995**, 52, 6431-6439.
- (82) Du, Y.-P.; Zhang, Y.-W.; Sun, L.-D.; Yan, C.-H. Efficient Energy Transfer in Monodisperse Eu-Doped ZnO Nanocrystals Synthesized from Metal Acetylacetonates in High-Boiling Solvents. *J. Phys. Chem. C* **2008**, 112, 12234-12241.
- (83) Ghosh, S.; Kumar K., U. M.; Bhaktha, B. N. S. Heat-treatment controlled structural and optical properties of sol-gel fabricated Eu: ZnO thin films. *Opt. Mater.* **2017**, 64, 288-294.
- (84) Senapati, S.; Nanda, K. K. Red emitting Eu:ZnO nanorods for highly sensitive fluorescence intensity ratio based optical thermometry. *J. Mater. Chem. C* **2017**, 5, 1074-1082.

- (85) Ahmed, S. M.; Szymanski, P.; El-Nadi, L- M.; El-Sayed, M- A. Energy-Transfer Efficiency in Eu-Doped ZnO Thin Films: The Effects of Oxidative Annealing on the Dynamics and the Intermediate Defect States. *ACS Appl. Mater. Interfaces* **2014**, 6, 1765-1772.
- (86) Mangalam, V.; Pita, K. Effect of the interaction distance on 614 nm red emission from Eu^{3+} ions due to the energy transfer from ZnO-nc to Eu^{3+} ions *Opt. Mater. Expr.* **2018**, 8 (10) 3115-3132.